UC Irvine
UC Irvine Previously Published Works

Title
An optimization of beta in the DIII-D tokamak

Permalink

Journal

ISSN

Authors
Lazarus, EA
Lao, LL
Osborne, TH
et al.

Publication Date

DOI

Copyright Information

Peer reviewed

An optimization of beta in the DIII-D tokamak

E. A. Lazarus,[a] L. L. Lao, T. H. Osborne, T. S. Taylor, A. D. Turnbull, M. S. Chu, A. G. Kellman, E. J. Strait, J. R. Ferron, R. J. Groebner, W. W. Heidbrink,[b] T. Carlstrom, F. J. Helton, C. L. Hsieh, S. Lippmann, D. Schissel, R. Snider, and D. Wroblewski[c]
General Atomics, P.O. Box 85608, San Diego, California 92186-9784

Accurate equilibrium reconstruction and detailed stability analysis of a strongly shaped, double-null, $\beta_T = 11\%$ discharge shows that the plasma core is in the second stable regime to ideal ballooning modes. The equilibrium reconstruction using all the available data (coil currents, poloidal magnetic loops, motional Stark effect data, the kinetic pressure profile, the magnetic axis location, and the location of the two $q = 1$ surfaces) shows a region of negative magnetic shear near the magnetic axis, an outer positive shear region, and a low shear region connecting the two. The inner negative shear region allows a large positive shear region near the boundary, even at low q ($q_{95} = 2.6$), permitting a large outer region pressure gradient to be first regime stable. The inner region is in the second stable regime, consistent with the observed axial beta [$\beta_T(0) = 44\%$]. In the low shear region p' vanishes, consistent with Mercier stability. This is one way to extend the ballooning limit in shaped plasmas while maintaining stability against external kinks. The $n = 1$ analysis shows that the plasma is unstable to an ideal internal mode, consistent with the experimental observations of a saturated internal $m/n = 1/1$ mode. The core plasma pressure, not being limited by ballooning stability, appears to be reaching a local equilibrium limit at the magnetic axis.

I. INTRODUCTION

Improved axisymmetric control on DIII-D[1] has allowed operation near the axisymmetric stability limit, enabling an increase in the achieved normalized current, I_N, at moderate q and leading to a record level volume average toroidal beta, β_T, of 11%. We have previously reported briefly on this experiment.[2] Here we discuss the experimental results in greater detail and present the ideal magnetohydrodynamic (MHD) stability analysis.

Scaling of experimentally achieved beta and calculations of the stability limits against ideal kink ($n = 1$, where n is the toroidal mode number) and ideal ballooning modes have shown theoretically and experimentally that the maximum toroidal beta in tokamaks scales with the normalized current,[3-5] $\beta_T^{max} \propto I_N$, $I_N \equiv I_p/aB_T$, where I_p is the total plasma current, a is the minor radius, and B_T is the toroidal field. Since disruptions or related instabilities set a lower bound to the safety factor, $q \approx RB_T/(\mu_o \bar{j}_T) f(\kappa, \delta)$, where $\bar{j}_T$ is the average toroidal current density and $f(\kappa, \delta)$ is an increasing function of elongation, κ, and triangularity, δ, I_N can be increased by increasing κ and δ, until limited by axisymmetric ($n = 0$) stability. In the experiment reported here, we operated simultaneously near the intersection of the $n = 0$ and $n = 1$ stability boundaries with a plasma shape that optimized the achievable I_N.

In previous work[6-8] we have demonstrated the capability of DIII-D to operate very near the ideal axisymmetric stability limit. This has enabled operation at elongation,

κ, up to 2.5. Also, we have achieved beta values in excess of 9% in the full-radius DIII-D double-null divertor configuration[5] (DND), where $\kappa \sim 2.1$ with triangularity $\delta \sim 0.9$. In this configuration, at low β the plasma is very near the marginal point for axisymmetric stability, however, at high beta ($\beta \sim 8\%$) the current profile (characterized by the internal inductance) becomes quite broad ($l_i \sim 0.8$), and then the plasma is no longer near the axisymmetric limit. This enables us to establish a high beta DND plasma and, during the high beta phase, adjust to a still more advantageous shape with higher κ, which is theoretically expected to result in an even higher beta limit. Due to the vacuum vessel geometry, $\kappa > 2.1$ is achieved by decreasing the plasma minor radius.

A major difference between the work reported in Ref. 5 and this work lies in the pressure profile. We find for our best plasma that $\beta(0) = 44\%$ at $q_{95} = 2.6$. We are defining $\beta(0)$ as the pressure at the magnetic axis normalized to the vacuum toroidal field value at the axis. This central pressure is well above the first stable ballooning limit. Such a high ratio of peak-to-average pressure is atypical of tokamak high beta experiments. About half the axial pressure is in the fast ion component. In the full-radius DND configuration with $\beta_T = 9\%$, we calculate that $\beta(0) = 16\%$ at similar q_{95}.

From analysis of the plasma equilibria we infer the magnetic shear profile and the plasma pressure profile. These profiles indicate a region of negative magnetic shear and high pressure near the magnetic axis, which is in the second stable regime to ideal ballooning modes, as is expected under these circumstances.[9] This region is surrounded by a low magnetic shear, vanishing pressure gradient region consistent with Mercier stability. Finally these
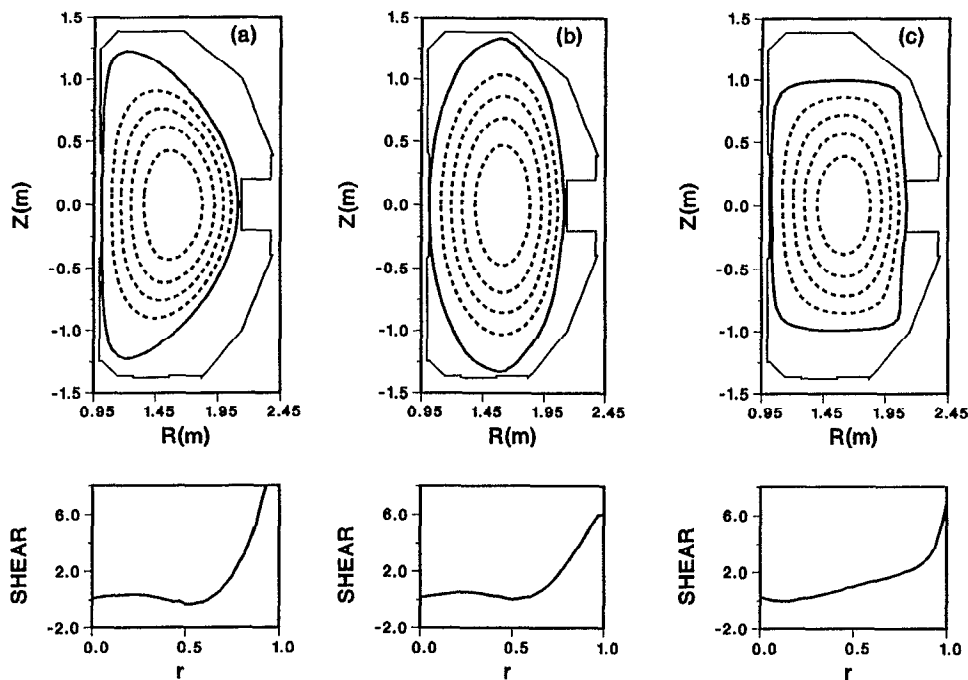
FIG. 1. A comparison of the stability properties of three shapes, all of which are near the marginal point for axisymmetric stability and feasible in DIII-D. Flux surface geometry and global shear are shown. For all cases $B_T = 1$ T and $q_{95} = 3.0$: (a) a "D" ($\mathscr{S} = 8.2$, $R_0 = 1.56$, $a = 0.55$, $\beta_p = 0.99$, $l_i = 1.00$, $\kappa = 2.2$, $\delta = 0.64$); (b) an ellipse ($\mathscr{S} = 7.7$, $R_0 = 1.57$, $a = 0.56$, $\beta_p = 0.98$, $l_i = 0.98$, $\kappa = 2.4$, $\delta = -0.03$); and (c) a rectangle ($\mathscr{S} = 6.1$, $R_0 = 1.57$, $a = 0.55$, $\beta_p = 0.98$, $l_i = 0.96$, $\kappa = 1.8$).

regions are surrounded by a region of positive magnetic shear with pressure gradient in the first stable regime.

In Sec. II we discuss the optimization of the plasma shape, and the procedure necessary for obtaining the high β high κ discharges. In Sec. III we present the experimental results and the analysis of the equilibrium. In Sec. IV we present the stability analysis. In Sec. V we discuss the possibility of an isodynamical equilibrium limit to central beta and offer evidence that this limit is encountered in the experiment. Section VI summarizes the experiment and provides an opportunity for our interpretation of the results.

II. SHAPE OPTIMIZATION

The experiment was based on the idea that maximum beta would be achieved in a plasma with an optimized shape as defined below. This optimized shape is constrained by axisymmetric ($n = 0$) stability. Since the axisymmetric limit is, to lowest order, independent of plasma current, we still have the freedom to chose the safety factor. The safety factor will then be limited by kink ($n = 1$) stability. We want to operate in this corner of parameter space defined by the intersection of $n = 0$ and $n = 1$ stability to maximize β.

In this section we illustrate this optimization procedure by defining a shape parameter, $\mathscr{S} \equiv I_N \cdot q$. Increasing $\mathscr{S}$ is equivalent to achieving the highest possible I_N at the highest possible safety factor, q, which is consistent with axisymmetric stability in DIII-D. For fixed $\mathscr{S}$ the maximum I_n, and hence β_T, is obtained at the minimum q. The minimum q value is set by disruption and related instabil-

ities. Although the value of q is somewhat affected by plasma shape and current density profile, it generally lies between 2 and 3. Here $\mathscr{S}$ is primarily a function of the geometry of the plasma surface, $\mathscr{S} \approx A^{-1}[(1 + \kappa^2 \cdot \mathscr{F})/2] \cdot [1 + \mathscr{O}(A^{-2})]$, where A is the aspect ratio and $\mathscr{F}$ is some function of the higher- (than quadrupole) order shaping fields. Note that $\mathscr{S}$ is more general than a simple specification of κ and δ, and takes into account the toroidal field weighting of the entire outer contour of the plasma. The advantage of dealing with $\mathscr{S}$ rather than I_N is that $\mathscr{S}$ is bounded by axisymmetric stability and is largely independent of q. As shown below, there is a maximum value of $\mathscr{S} = 8.25$ for DIII-D and the only consideration in deducing this maximum is axisymmetric stability.

The flexibility of the DIII-D poloidal coil system allows a wide variety of shapes. We consider as illustrations of the optimization of $\mathscr{S}$, with respect to $n = 0$ stability, an ellipse, a "D," and a rectangle (Fig. 1). All three are, in principle, achievable in DIII-D, as they must be if we are to evaluate the axisymmetric stability using the real vessel wall. While this illustration is not offered as proof that maximum $\mathscr{S}$ results in maximum beta, it is intended to make this hypothesis plausible to the reader.

The constraint of axisymmetric stability is only meaningful if l_i is specified. On DIII-D we find that H-mode plasmas have l_i values in a narrow range with little sensitivity to the safety factor, so we will constrain the value of l_i at 1.0, a value typical of H-mode plasmas. The definition of l_i employed here is $l_i \equiv (\oint_S dl)^2 \int_V B_p^2 \, dV / [V(\oint_S B_p \, dl)^2]$. In the illustration we hold the major and minor radii constant at 1.57 and 0.55 m, respectively. Here q_0 is con-

TABLE I. Beta limits for three plasma shapes optimized against axisymmetric stability.

	"D"	Ellipse	Rectangle
$\mathscr{S}$	8.2	7.7	6.1
$\beta_T^{\text{ballooning}}(\%)$	8.6	7.1	5.7
$\beta_T^{\text{kink}}(\%)$	16.1	11.2	1.9
I_p (MA) at $q_{95}=3$	1.51	1.42	1.11

strained to be 1.05, and I_p is set to provide $q_{95}=3$ at $B_T=1$ T. Each shape is determined by the constraint that the equilibrium be within 5%–10% of the ideal axisymmetric stability limit. The definition of the margin of vertical stability is that used in Ref. 8. The ideal MHD axisymmetric stability limit is computed with GATO.[10]

For each shape an equilibrium is calculated, where the pressure profile is everywhere at the marginal point for infinite-n ballooning modes. Additionally, the external kink limit ($n=1$) is calculated by globally scaling that pressure profile, while keeping the shape and l_i fixed. Thus we obtain a high-n and a low-n beta limit for each shape. The equilibria are shown in Fig. 1, along with the shear profiles. Results are summarized in Table I below. We shall frequently use the variable r as the normalized minor radius, where $r \equiv \sqrt{V(\tilde{\psi})/V(1)} \approx \sqrt{\tilde{\psi}}$, V is plasma volume, and $\tilde{\psi}$ is the normalized poloidal flux enclosed by a flux surface.

Not surprisingly, we find that optimization requires minimizing the quadrupole and octopole components of the external field while maximizing the hexapole component, thereby improving the average curvature. Also, we see in Fig. 1, that as $\mathscr{S}$ is increased under conditions of fixed q_0, q_{95}, and l_i, the region of strongest shear moves toward the edge of the plasma. Thus, the region able to support the largest $p'(\psi)$ against ballooning modes moves toward the edge, and because of the volume effect this leads to a higher average β_T. In the central region, because of low shear, p' is severely limited, leading to a rather flat pressure profile. For the rectangular shape the $n=1$ limit is well below that for ballooning modes, while for the "D" the opposite is true.

Having established the general characteristics of the optimized shape we turn to the specific design of this experiment. Our optimization procedure begins with shot 66493, discussed in Ref. 5, which reached $\beta=9.3\%$. The internal inductance for this plasma was $l_i \approx 0.8$ and we shall use this as a constraint, along with the specification that $q_0=1$. We will choose as a pressure profile the one that is marginally stable to infinite-n ideal ballooning modes. Because of the vessel shape κ can only be increased by reducing the minor radius. We increase κ while reducing R_0 (and thus limiting the increase in the aspect ratio) until we achieve a marginal condition for axisymmetric modes. We maintain a diverted plasma in order to achieve the H mode. The final result of the designed equilibrium is shown in Fig. 2. We find we can achieve $\mathscr{S}=8.25$, which is to be compared with $\mathscr{S}=7.25$ for shot 66493. The two shapes
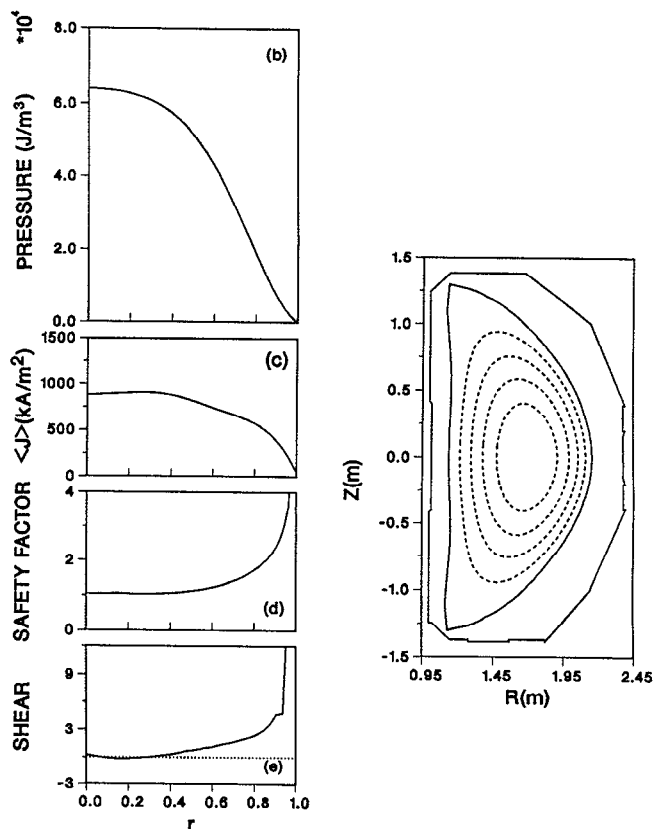

FIG. 2. The beta-optimized equilibrium we seek to produce experimentally. This equilibrium is within 2% of the axisymmetric limit, has a pressure profile that is marginal to ballooning mode and is slightly beyond the $n=1$ stability limit. Here $q_{95}=3.1$, $\beta_N=4.3$, $I_N=2.66$, $\kappa=2.50$, $l_i=0.79$, and $n/n_c=0.92$: (a) Flux surface contours; (b) the pressure versus normalized radius defined by $r \equiv \sqrt{V(\tilde{\psi})/V(1)} \approx \sqrt{\tilde{\psi}}$; (c) the flux surface averaged toroidal current density versus r, and (d) the safety factor versus r; and (e) the shear versus r.

are compared in Ref. 2. After establishing this shape with the marginal ballooning pressure profile, we evaluate $n=1$ stability and find the plasma is slightly unstable (i.e., the displacements are small enough at the boundary so we do not believe the plasma would disrupt) to $n=1$ modes. We note that the margin for axisymmetric stability is being reduced both by the increase in κ and the decrease in R_0, which increases the distance from the plasma to the outer wall of the vessel. This is the region of the wall that provides most of the vertical passive stabilization.

The current density profile shown in Fig. 2(c) is somewhat hollow. This is a result of the strong shaping and the constraints of fixed l_i and q_0. Since the field shaping coils primarily affect the shape of the outer flux surfaces, κ generally decreases from the plasma boundary inward, and, from equilibrium constraints, $\delta=0$ at the magnetic axis. Since $q \approx RB_T/(\mu_0 \bar{j}_T)f(\kappa,\delta)$, increasing κ at constant q on the boundary and $q_0=1$ ultimately produces a hollow current density profile. As we continue to increase the shaping in the model equilibria, and/or lower the aspect ratio (at constant safety factor and constant l_i), the minimum in q moves away from the axis, and we can no longer find equilibria with monotonic q profiles.
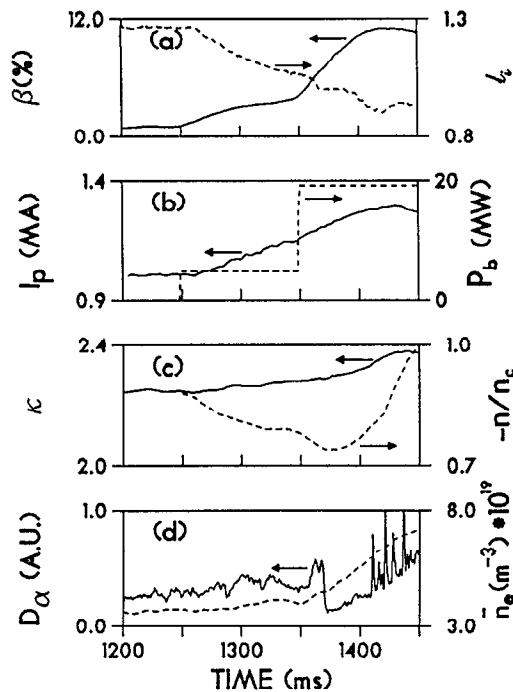
FIG. 3. The time evolution of 69608. The plasma disrupted at 1462 msec. (a) β_T and l_i; (b) plasma current and neutral beam heating; (c) κ and n/n_c; and (d) D_α emission showing the H-mode transition and line-averaged density.

The constraints on this equilibrium are quite severe; the plasma pressure is at the ballooning limit and the convergence of the kink and axisymmetric stability limits excludes the possibility of any significant change in the current profile, in that a narrowing (higher l_i) will destabilize axisymmetric modes, while a broadening (lower l_i), or an increase in β, will destabilize the external kink.[11] The beta of this equilibrium is 11.4%. The ballooning marginal pressure profile is quite broad, with $p_0/\langle p \rangle = 2$. The goal of the experiment is to produce the plasma shown in Fig. 2.

III. EXPERIMENTAL RESULTS

The primary effort in this experiment was to achieve a high degree of up–down symmetry and time the shape evolution to keep the reduced decay index,[6] n/n_c, which measures the vertical stability margin constant at $n/n_c \approx -0.9$ as β increases. Based on previous work[7] as well as the stability analysis of the design plasma, we expect for this shape that this value of n/n_c represents the ideal limit. Any loss of up–down symmetry represents a waste of axisymmetric stability, in that the quadrupole field is being increased, but the sought for maximum average curvature is not achieved. The shape control system was adjusted to reduce up–down asymmetry to less than 1%. The vertical control system was tuned to have a very high derivative gain for optimal performance.

A. Time evolution of highest beta shot

Figure 3 shows the time history of shot 69608 beginning just before the start of beam heating. This shot

reached 11% beta. Here we show the plasma current, the neutral beam timing, the rise in β and decrease in l_i, the evolution of κ and n/n_c, and the divertor D_α and the line-averaged electron density. The control of the current profile is affected first by the I_p ramp, then by the increase in β itself with additional heating power, then by the transition to the H mode, as indicated by the drop in the D_α light at 1370 msec. The increase in κ is programmed to roughly match the decrease in l_i. As indicated by n/n_c, we remain a safe distance from axisymmetric instability through the high beta phase of the shot, but n/n_c is decreasing to -1 by the end of the shot. The density rises throughout the beam-heated phase in an uncontrolled fashion, as is typical for H-mode plasmas. The plasma disrupted at 1462 msec, exhibiting a rapidly growing ($\gamma \approx 30~\mu\text{sec}^{-1}$) $n = 1$ instability. The thermal quench was completed in approximately 200 μsec. A slowly growing $m/n = \frac{3}{2}$ mode appears on the magnetics beginning at 1435 msec and may contribute to the later disruption. One notable feature is that the onset of the edge-localized modes (ELM's) did not result in a beta collapse. In the full-radius DND configuration ($\kappa \approx 2.1$, $\delta \approx 0.9$) at high beta the first ELM results in either a disruption or a sharp reduction in beta.

B. Comparison of shots 69608 and 69609

We now turn to a discussion of the following shot 69609. The reasons for this are twofold; first, the differences highlight special features of the highest beta result, and second, we did not obtain Thomson scattering data for 69608 and will need to use the density profile data from 69609 in order to calculate the fast ion component of the pressure and the pressure profile for 69608. The difference in discharge programming between the two shots was slight; only minor tuning of power supply voltages was done in order to better control plasma shape. We show the relevant diagnostic set for this experiment in Fig. 4.

Shot 69609 only achieved a β_T value of 9.2%, similar to earlier results.[5] As can be seen from Fig. 5 the discharges have very similar parameters, until a large sawtooth occurs in 69609 at 1375 msec during the high-power beam phase. At the sawtooth the neutron rate drops by 27% in 1.5 msec. This rapid drop in neutron rate cannot be due to a drop in ion temperature since the thermal deuterons contribute negligibly to the neutron rate in 69609. A drop in electron temperature would reduce the neutron rate on the fast ion slowing down time, which is about 50 msec in shot 69609 and therefore too slow to explain the rapid drop observed. At the time of the sawtooth crash about 50% of the plasma stored energy is in fast particles. There is no significant change in plasma stored energy at the sawtooth, indicating that there is no significant loss of fast or thermal particles. It seems likely then that the sawtooth in 69609 flattens the initially centrally peaked fast ion distribution, thus reducing the beam–beam interaction neutrons that account for about 50% of the neutron rate. Such a flattening has been observed in the Joint European Torus (JET).[12] Following the sawtooth the plasma stored energy increases much more slowly than in shot 69608 [Fig. 5(a)]. This could be due to either a reduction in the
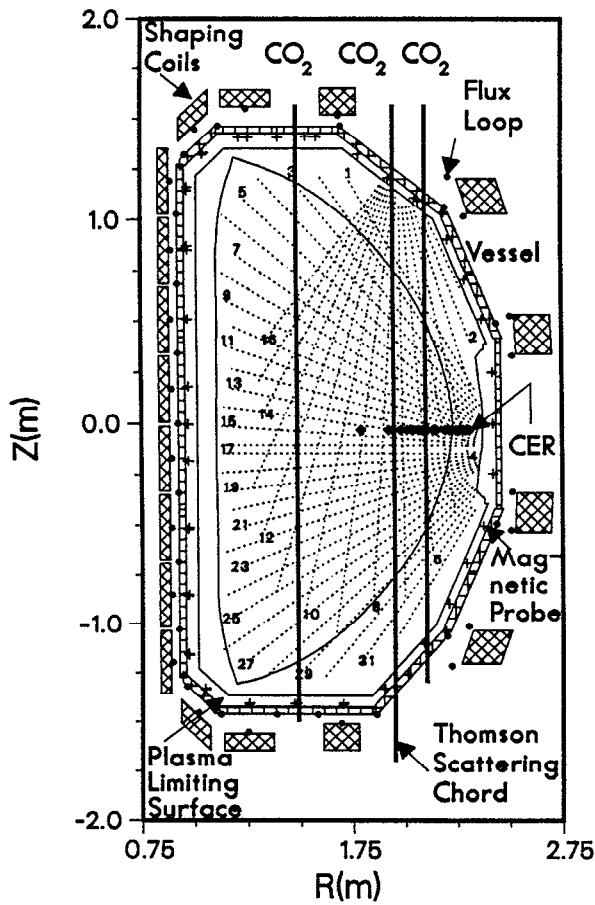
FIG. 4. DIII-D with the diagnostic set pertinent to this experiment. Shown are the top and side SXR arrays, including the numbering conventions, the three CO_2 chords, along which the electron density is measured, the Thomson viewing chord, the CER viewing points (diamonds) for T_i, the magnetic probes ($+$), flux loops (solid circles) and shaping coils, each of which has a Rogowski coil for current measurement. The boundary of a plasma typical of this experiment is drawn in. The magnetic axis of these plasmas will be quite close to the innermost CER point.
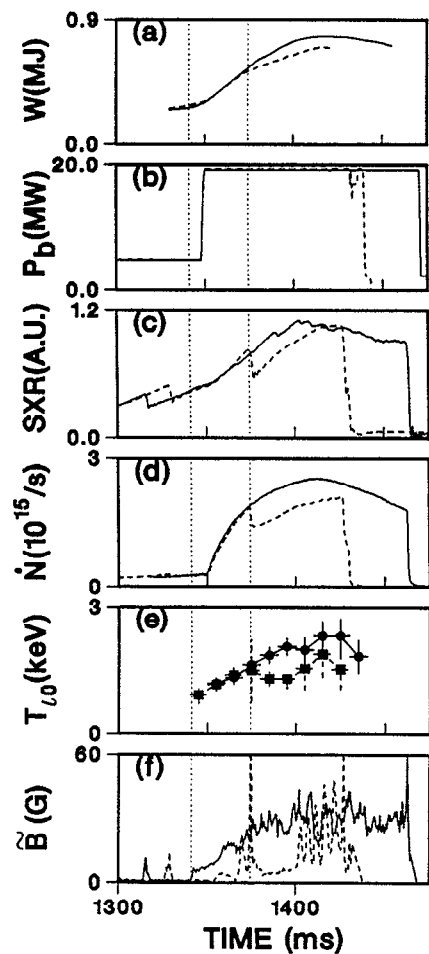
FIG. 5. A comparison of the time evolution of 69608 and 69609. (a) Plasma stored energy; (b) neutral beam heating power; (c) a central soft x-ray chord; (d) neutron rate; (e) central ion temperature; and (f) the amplitude of the $m/n = 1/1$ component of B_p as seen at the outside midplane. The dotted vertical lines are at 1342 and 1375 msec. The bursts of $m/n = 1/1$ activity for 69609 beginning at 1400 msec are fishbone oscillations.

energy confinement time or a reduction in the effectiveness of the heating due to the inferred spatial flattening of the fast ion distribution.

At 1400 msec in shot 69609, fishbone oscillations[13] begin, which can be seen as bursts in magnetic fluctuations in Fig. 5(f). The fishbone oscillations impede the increase in neutron rate in this shot.

Sawteethlike events are also observed in the higher β discharge, 69608, however these are much smaller in amplitude than in shot 69609 and have no noticeable effect on the neutron rate. Figure 6 shows a comparison of the change in soft x-ray amplitude profile at the sawtoothlike event near 1390 msec in shot 69608 with the sawtooth at 1375 msec in shot 69609. The inversion radius is smaller in the higher beta shot and the profile remains relatively peaked, even within the inversion radius. The change in the amplitude of the soft x-ray (SXR) signals is significantly smaller across the central channels in shot 69608 compared to 69609 (Fig. 6). A reconnection process limited to an annular region[14,15] could still explain this data if the tem-

perature gradient in the region were sufficiently large, since the SXR path length between flux surfaces decreases with increasing minor radius, while the volume between flux surfaces is relatively independent of flux near the $q = 1$ surface.

The rolloff in neutron rate, central SXR signal, and stored energy in shot 69608 corresponds in time to the start of ELM's (Fig. 3). The ELM's have a pronounced effect on the edge SXR channels, which are rising rapidly before the onset of ELM's, and are subsequently clamped or decline, suggesting a sharp reduction in the confinement of the outer part of the plasma cross section.

We now turn to the detailed discussion of the saturated internal mode that dominates shot 69608. At 1342 msec, during the secondary plasma current ramp but before the high-power injection phase, a MHD mode suddenly appears and remains relatively saturated for the rest of the shot [Fig. 5(f)]. This mode has a $m = 2$, $n = 1$ structure on the magnetics and a frequency of 9.2 kHz, which corre-

3648   Phys. Fluids B, Vol. 4, No. 11, November 1992
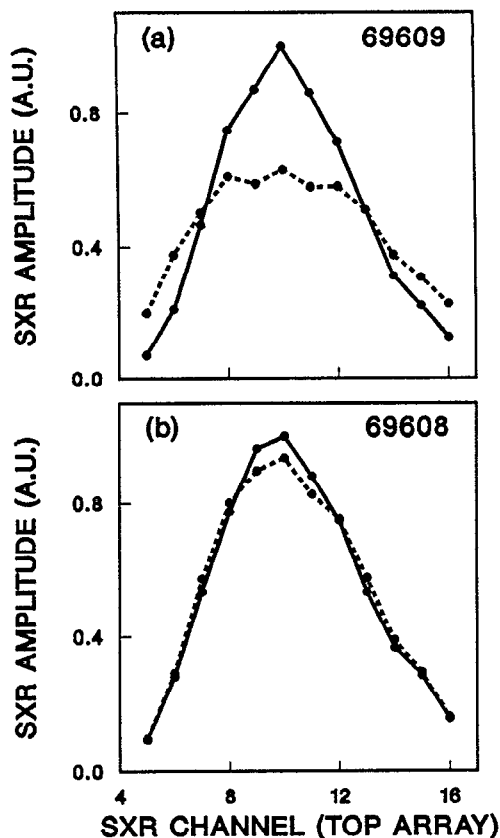
Lazarus et al.   3648

FIG. 6. The change in the x-ray emissivity profile after (a) the sawtooth crash of 69609 at 1375 msec, and (b) the sawtoothlike event of 69608 at 1390 msec. The solid line is before the sawtooth and the dashed line immediately after.
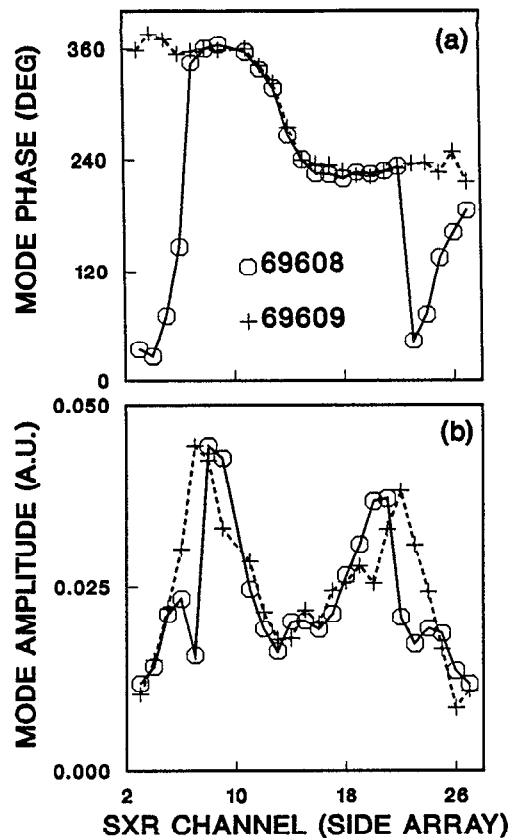
FIG. 7. Comparison of phase and amplitude variation of the $m/n=1/1$ modes, as deduced from the SXR signals. The solid line is from shot 69608 and the dashed line is from shot 69609.

sponds to the central rotation speed measured by charge exchange recombination (CER). At this same frequency a mode is observed on the soft x-ray arrays. The poloidal variation of the phases of the SXR data indicates this mode has $m=1$. This suggests that the internal mode is also $n=1$ and that the $m=2$, $n=1$ mode observed on the magnetics is driven by a coupling to the internal $1/1$ through the noncircular cross section and toroidicity.

During the sawtooth on shot 69609 a precursor oscillation is observed on the magnetics and SXR. This precursor has $2/1$ character on the magnetics and $m=1$ character on the SXR, with a frequency of 10.6 kHz. The amplitude of the sawtooth precursor just before the sawtooth crash is approximately twice the amplitude of the continuous mode. The ratio of amplitude of the mode on the SXR to the outboard midplane magnetic probe is the same for the continuous mode and the sawtooth precursor.

Detailed analysis of the SXR emission from 69608 implies the existence of two $q=1$ surfaces. Figure 7 shows a comparison of the variation of phase and amplitude across the SXR channels. Although the plasma current is somewhat higher and the internal inductance is somewhat lower in shot 69608 at the time of the sawtooth at 1390 msec compared to shot 69609 at the time of its sawtooth at 1375 msec, the peak in the mode amplitude and sawtooth inversion radius is at substantially smaller minor radius. An

additional peak at larger minor radius can be seen in the fluctuation amplitude for the case of the continuous mode; also, there is a jump in phase of approximately 180° between the large and small peaks, which does not occur in the case of the sawtooth precursor. Although the $m=1$ mode decreases in amplitude and appears to shift in radial location at the sawtooth drops in shot 69608, the mode is not eliminated. The two $m=1$ mode remain locked in phase with their O points separated by 180° poloidally. The $m=1$ mode in shot 69608 never appears strongly on the channel, corresponding to the plasma center; it does, however, appear on the central channel during the sawtooth crash of shot 69609. These data suggest that the model applied to compound sawteeth,[15] in which two $q=1$ surfaces exist in the plasma, and the central q value is too far above unity to allow reconnection to proceed to the plasma center, may also apply to shot 69608.

Confirmation of the existence of the two $q=1$ surfaces is obtained by examining the phase shifts of the first harmonic frequency. In simple simulations (unshifted circles) one finds that 180° phase jumps in the harmonic occur when the island O point crosses a viewing chord, and the harmonic has no phase jump across the plasma center. As indicated by the arrows in Fig. 8 two such phase jumps occur for 69608, and these are observed above and below
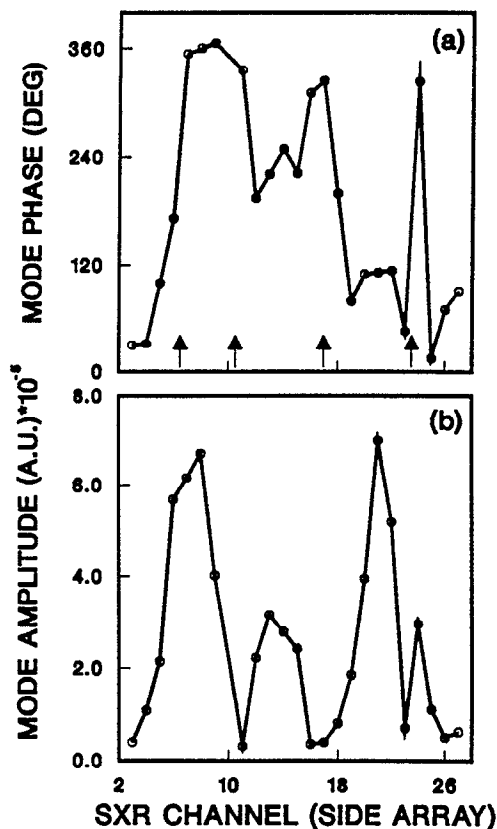
FIG. 8. Phase and amplitude variation of the first harmonic of the m/n = 1/1 modes, as deduced from the SXR signals. The arrows point to the phase jumps that occur across island O points.

the midplane. The phase variation across the plasma center is continuous.

We have assumed that the partial reconnection model applies and that the peaks in the 1/1 mode amplitude correspond to the location of the two $q=1$ surfaces. These $q=1$ locations are applied as additional constraints to the equilibrium fits for shots 69608 and 69609.

Each fishbone in shot 69609 results in about a 2% decrease in the neutron rate. The fishbones are 1/1 modes with frequency of 11 kHz. Although the continuous 1/1 mode in shot 69608 is of similar amplitude and frequency to the fishbone oscillations, it does not appear to affect the neutron rate in shot 69608, as is evidenced by the somewhat higher neutron rate in shot 69608 compared to 69609 before 1375 msec. We conclude that the $m/n=1/1$ mode in shot 69608 is not the fishbone instability.

The internal $m/n=1/1$ mode first appears and saturates 10 msec before the high beam power phase of the high β shot. The growth rate prior to saturation is 530 μsec^{-1}. Other sawteeth during the low-power beam injection phase of 69608 and 69609 show a period of saturation of up to 2 msec duration followed by a rapid growth for about 0.5 msec and the sawtooth crash. The longest period of saturation during the low beam power phase occurs for the sawtooth, which comes latest in the discharge. This suggests that the mechanism responsible for the saturated 1/1
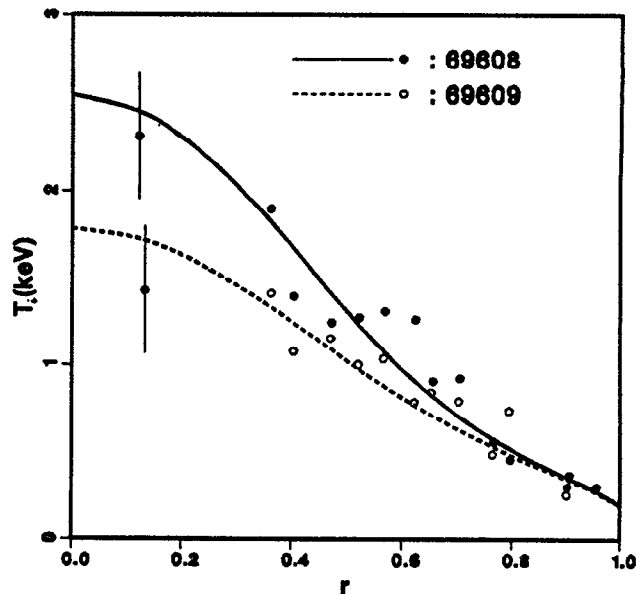

FIG. 9. A comparison of T_i vs r for 69608 and 69609 at the times of maximum beta. Shot 69608 at 1417 msec is shown as the solid circles and a solid line. Shot 69609 at 1400 msec is shown as the open circles and dashed line. The lines are statistically weighted smooth spline fits to the data and are used as input to the ONETWO[21] code for the calculation of total pressure.

mode in shot 69608 may be present to some extent in both shots before the high-power beam injection phase. Because of this observation and the fact that the shots 69608 and 69609 have very similar β_p, l_i, and heating power up to the time of the large sawtooth in shot 69609; it is difficult to attribute the saturation of the 1/1 mode and the lack of large sawteeth in shot 69608 to the effects of fast particles, as has been done on other experiments.[16]

C. Profile analysis and equilibrium reconstruction

The MHD equilibrium for discharges 69608 and 69609 at the time of highest β are reconstructed from the measured thermal pressure profile data, the computed fast ion pressure, the motional Stark polarimetry data, the location of the two $q=1$ surfaces as determined from SXR emission, the diamagnetic data, the external poloidal magnetic data, and the currents in the poloidal coils.[17]

The difference in central MHD activity translates into an 800 eV difference between 69608 and 69609 in central ion temperature, as shown in Fig. 9. Notice that outside of $\rho \approx 0.4$ there is little difference in T_i between the two plasmas. The temporal evolution of the density as well as the ratio of the density along different chords was very similar, indicating that there was a very small difference in the shape of the density profile. The D_α level was also identical. There is no observable difference in the shape. This provides the basis for using n_e from 69609 in reconstructing 69608. The purpose in doing so is to obtain a calculation of the fast ion component of the total pressure. There were several shots in this series as κ was increased, and all showed similar density profiles with a large peak in the outer region. The n_e profile data (Fig. 10) from 69609 are
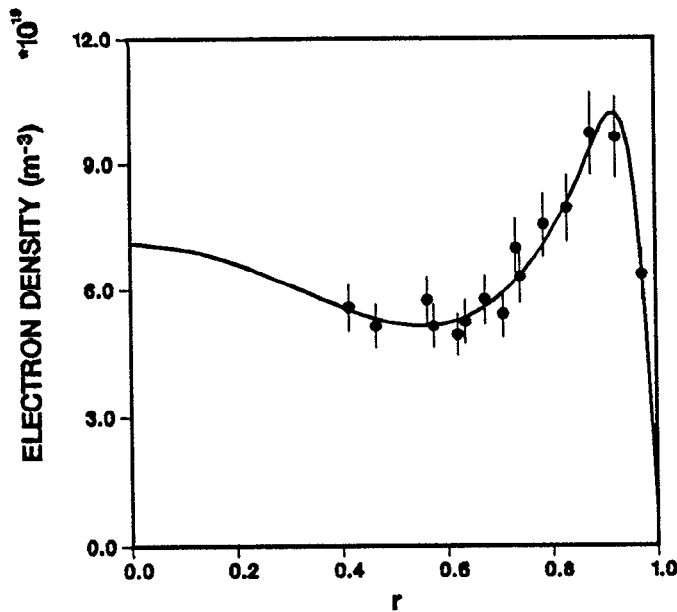
FIG. 10. Density profile used for kinetic analysis of 69608. The points of relative density are Thomson scattering data from 69609 renormalized to the line-averaged density of 69608. The spline fit is constrained to match the three line-integral density values of shot 69608.
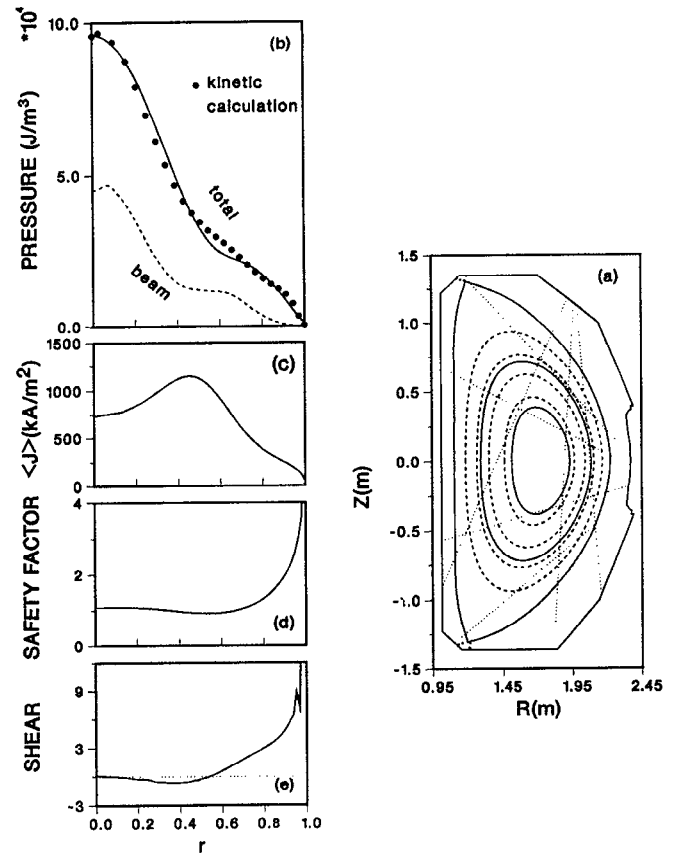

FIG. 11. Equilibrium reconstruction for 69608. (a) Flux surface contours. The inner solid contours are the $q=1$ surfaces and the dotted lines are the soft x-ray chords on which the peak $m/n=1/1$ activity is observed. (b) The pressure versus normalized radius. The solid line is the best fit in the equilibrium reconstruction, the solid circles are the total pressure, which is the sum of the measured thermal and calculated fast ion component, and the dashed line is the calculated fast ion component. (c) The flux surface averaged toroidal current density, (d) the safety factor, and (e) the shear.

normalized to the line-averaged density (three chords) from 69608. The density in 69608 was 15% higher than that of 69609. We also use the approximation $T_e = T_i$, which is justified by the high density. In 69609 for the region $\rho \gtrsim 0.4$, where both T_e and T_i data exist, they are the same within experimental accuracy.

The lines are on this and the following figure are spline fits through the data that are used as input to the calculation of the fast ion component of pressure. Compared at their times of peak beta, the soft x-ray emissivity profiles indicate that in addition to the ion temperature, the electron pressure is more peaked for 69608. The inverse bremsstrahlung measurement yields $Z_{\mathrm{eff}} \approx 1.3$ for these plasmas, and this is consistent with the spectroscopic survey. The vessel had been carbonized[18] three days prior to this experiment, and this is likely the reason for the plasma cleanliness. As expected for these conditions, the dominant impurity was carbon.

The axial safety factor $q(0)$ is also constrained to match the location of the inner $q=1$ surface, as inferred from the SXR channels of peak fluctuation amplitude. For discharge 69608, as discussed in the previous section, there are two $q=1$ surfaces located inside the plasma. Therefore, for this shot, $q(0)$ is constrained to be above 1 with a value to match the location of the inner $q=1$ surface to the appropriate SXR chords. For discharge 69609, there is only a single $q=1$ surface and $q(0)$ is constrained to be below 1 with a value to match the location of the $q=1$ surface, as is usually done. Additional information on the q profile is provided by the motional Stark diagnostic,[19,20] which gives a single point measurement of the local field line pitch angle. For the shots discussed here, the measurement was made at $R=1.97$ m and $Z=0$, between the $q=1$

surfaces. The pitch angle corresponds to a q value of 0.95, consistent with the q profile. The results for 69608 are shown in Fig. 11. The main plasma parameters are given in Table II.

TABLE II. Plasma parameters for DIII-D discharges 69608 and 69609 at $t=1417$ and 1400 msec.

	69608	69609
Major radius, R_0 (m)	1.66	1.66
Minor radius, a (m)	0.557	0.560
Elongation, κ	2.35	2.35
Triangularity, δ	0.84	0.84
Toroidal beta, β_T (%)	11.3	9.2
Central beta, $\beta(0)$ (%)	44	≈ 16
Poloidal beta, β_P	0.96	0.83
Internal inductance, l_i	0.91	0.91
q (0.95)	2.6	2.6
Beam power (MW)	19.2	19.4
I_p (MA)	1.28	1.26
B_T (T)	0.75	0.75

As described in the previous experimental section, there is no evidence for fast ion redistribution for discharge 69608, although discharge 69609 does show signatures of fast ion redistribution due to sawteeth and fishbone oscillations. Thus, in the equilibrium reconstruction, for discharge 69608 the entire pressure profile is constrained to match the total pressure data, including the fast ion component, whereas for discharge 69609 only the pressure profile outside of the $q=1$ surface is constrained to match the pressure data, and in the central region where q falls below 1 it is allowed to redistribute across different surfaces.

The volume average toroidal beta, β_T, for discharge 69608 is 11.3%, with one-third contributed by the fast beam ions. The central toroidal β for this discharge is approximately 44%, with about one-half contributed from fast beam ions. As shown in Fig. 11(b), the fast ion and total pressure profiles are very peaked near the center, with half of the central pressure gradient coming from the fast beam ions. This extremely peaked central pressure results in closed total magnetic field strength, B, contours in the central region for discharge 69608. This feature will be discussed further in Sec. V. The q profile that allows the best match of the $q=1$ surfaces to the soft x-ray data is slightly hollow with $q(0)=1.1$, as shown in Fig. 11(d).

As described in Ref. 18, the thermal component of the total pressure is directly obtained from the measured profile data, whereas the fast component from the beam is estimated analytically using a standard classical slowing down model.[21] The fast ion pressure is computed using NFREYA[22] for beam deposition and an analytical Fokker–Planck slowing down calculation in the equilibrium geometry. We have separately performed a Monte Carlo slowing down calculation, which yields a similar, but slightly more peaked, fast-ion component. The model assumes the slowing down of the fast ions occur in a time scale much faster than their radial diffusion time and hence the fast ions are confined near the flux surfaces, where they are born. There is experimental evidence that the slowing down process is near classical.[23,24] At modest beam power, in plasmas that are not near the beta limit, fast ion transport is observed to be approximately neoclassical.[25–27] The question of fast ion slowing down and radial transport in plasmas with intense neutral beam heating, which are near the beta limit, is not yet resolved. Because of the large contribution of the fast beam ions to the pressure in the central region, there is a systematic uncertainty in the calculated central pressure. At the same time, the fast ion pressure calculation must be globally correct, since it accounts for the 33% of the total pressure, and this contribution is needed to obtain agreement with the magnetics data. That is, equilibrium reconstruction using only poloidal field and flux measurements, or including the diamagnetic flux, agree in total stored energy with equilibria constructed, including the experimental thermal plus computed fast ion pressures. We note that β_P and l_i can be separately determined from the external poloidal magnetic field and flux measurements alone in elongated equilibria.[28]

In 69608 the instabilities normally responsible for fast ion redistribution that would invalidate the classical slow-ing down model calculation of the fast ion pressure are absent. A likely candidate for redistribution of fast ions is the fishbone instability; there were no fishbones in discharge 69608. Another possibility is the expulsion of fast ions in the sawtooth reconnection; however, 69608 had no such reconnection.

Nevertheless, the lack of a direct measurement of central pressure is a cause of concern in the evaluation of central beta. Fortunately, at high κ, the peakedness of the pressure profile can also be determined from the Shafranov shift of the magnetic axis. This shift can be determined from the soft x-ray emission profile. The location of the magnetic axis is sensitive[29] to both l_i and the shape of the pressure profile. It can be shown, using form factors $p(x)=p_0(1-x^2)^\mu$ and $J(x)=J_0(1-x^2)^\nu$ for pressure and current density, respectively, where x is the normalized minor radius, and Eqs. (3.9) and (3.10) of Ref. 29, that in the large aspect ratio, circular limit the shift of the magnetic axis, Δ_m is given by

$$\frac{\Delta_m}{a}=\frac{a}{2R}\left(\beta_p\int_0^1 2x\right.$$

$$\left.\times\frac{[1-(1-x^2)^{\mu+1}-(\mu+1)x^2(1-x^2)^\mu]}{[1-(1-x^2)^{\nu+1}]^2}dx+\frac{l_i}{2}\right),$$

$$(1)$$

$$\frac{\Delta_m}{a}\approx\frac{a}{2R}\left(\beta_p\frac{p_0}{\langle p\rangle}f(l_i)+\frac{l_i}{2}\right),\qquad(2)$$

where $f(l_i)$ is a function of l_i such that the pressure gradient contribution to the shift increases as l_i decreases. This expression emphasizes the point that the shift between flux surfaces is caused by the gradient in the pressure along with the gradient in the current density. Since l_i and β_p can be determined separately for elongated equilibria, the magnetic axis shift is a direct measure of the pressure profile peaking.

Experimentally, the axis location can be determined from the SXR emission profile. In Fig. 12 we show the location of the magnetic axis for such equilibrium fits as a function of the peaking factor, $p_0/\langle p\rangle$. The equilibrium identified by the dashed vertical lines is that of Fig. 11, the dashed line to the left is the location of the center of the inner $q=1$ surface, and the one to the right is the location of the magnetic axis. The scatter in these points from a smooth curve arises from forcing three choices, $q_0=0.3$, 0.7, and 1.0 in fitting the data. As can be seen the results are quite insensitive to the assumption made for q_0.

For the reconstructed equilibria of Fig. 11 if we then do the line integrals of $n_e^2(\psi)T_i(\psi)$ along the SXR chords the calculated and measured emission profiles are in good agreement (Fig. 13), confirming the location of the magnetic axis and hence the central beta value.

We note that the rotation velocity is small $(v_\phi \ll v_{T_i})$, as is the pressure anisotropy, as evidenced by the agreement of the diamagnetic and equilibrium beta measurements and as expected for the beam injection angles on DIII-D.

The axis location was based on the relative amplitude of the soft x-ray emissivity on the various viewing chords.
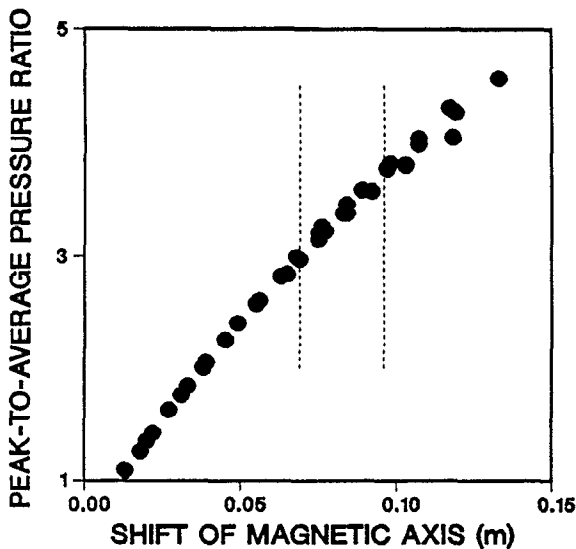
3652   Phys. Fluids B, Vol. 4, No. 11, November 1992

Lazarus et al.   3652

FIG. 14. A new spline fit to the T_i data, which is forced to match the flat spots corresponding to the $m/n = 1/1$ island structure.

FIG. 12. The magnetic axis shift versus $p_0/\langle p\rangle$. The dashed vertical line to the left is the location of the center of the inner $q=1$ surface, and the one to the right is the location of the magnetic axis.

The inner $q=1$ surface location was identified based on the spatial location of the peak in the fluctuation amplitude. If we assumed the pressure profile was flat within $q=1$, the shift would only be that of the $q=1$ surface from which we would infer $\beta(0)=33\%$ as a minimum central value. However, since there is clear evidence (Figs. 9, 10, and 13) that the pressure continues to rise within this $q=1$ surface, then Eq. (2) tells us that the average beta inside the inner $q=1$ surface is 33%. Based on these results, we have high confidence in the calculated central beta value of 44%.

Stability analysis of the equilibrium shown in Fig. 11 is problematic because most of the plasma in the region $0.33 \gtrsim \rho \gtrsim 0.7$ surface is ballooning or Mercier unstable. In the stability analysis of either this equilibrium or the one to
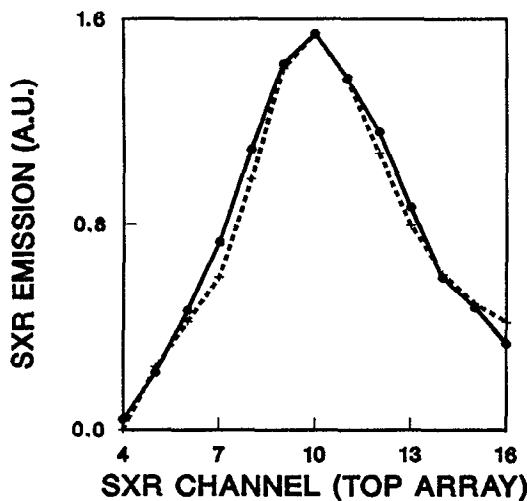

FIG. 13. The measured emissivity profile (solid line) and the line integrals of $n_e^2 T_i$ (dashed line) along the soft x-ray chords for 69608. The geometry is that of Fig. 11, the T_i profile is shown in Fig. 9, and the n_e profile is shown in Fig. 10.
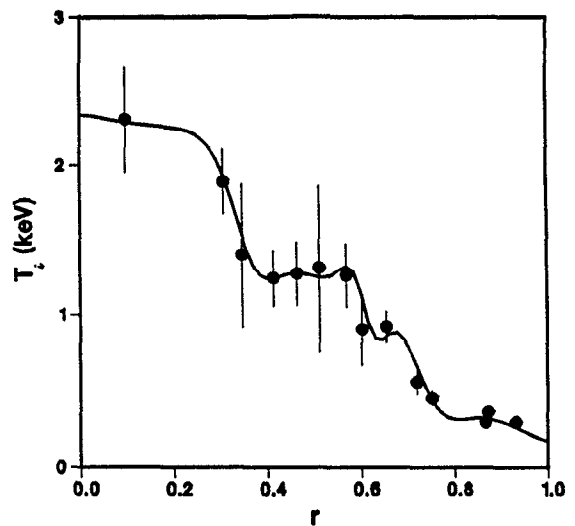
be presented below, the region within the inner $q=1$ surface is second stable as the shear is negative. Also, in either case, the region $\rho > 0.7$ lies within the first stable boundary. The difficulty lies in the transition to the first stable region.

Examining Fig. 9 more closely, we see distinct flat regions in the ion temperature profile ($0.4 \lesssim r \lesssim 0.6$, $0.63 \lesssim r \lesssim 0.7$) at locations corresponding to these islands. We then generated a new equilibrium, which accounts for these flat regions. The final fit to the T_i data is shown in Fig. 14.

We have found the generation of the equilibria to be exceptionally difficult. The equilibrium shown in Fig. 11 represents a free-boundary least-squares fit to the experimental data using the EFIT[17] code. For a pressure profile consistent with T_i from Fig. 9, EFIT exhibited the numerical analog to a vertical instability, which required a special technique to achieve convergence, as described in Ref. 2. For a pressure profile consistent with T_i from Fig. 14, our scheme for vertical stabilization of the fit fails to allow sufficient convergence of the solution for stability analysis. An attempt at fixed boundary calculations also failed as the equilibrium calculation fails to converge because the interior of the plasma still exhibits a growing vertical oscillation. We were able to find a sufficiently converged equilibrium only by imposing a constraint of symmetry about the midplane on each iteration. Although a significant effort was made to symmetrize the experimental plasma (the up–down flux ratios were adjusted to 1% accuracy) the symmetry constraint forces us to move from a reconstruction based on a fit (χ^2 minimization) to experimental data, to a calculation, where we shall enforce certain conditions based on that reconstruction. In generating the symmetrized equilibrium to match the revised pressure profile, we consider it important to preserve the following features, which are important characteristics of the experimental results: (1) total plasma current, (2) the tangency radii of the soft x-ray chords to the $q=1$ surfaces, (3) the boundary shape, (4) the internal inductance, and (5) the mag-
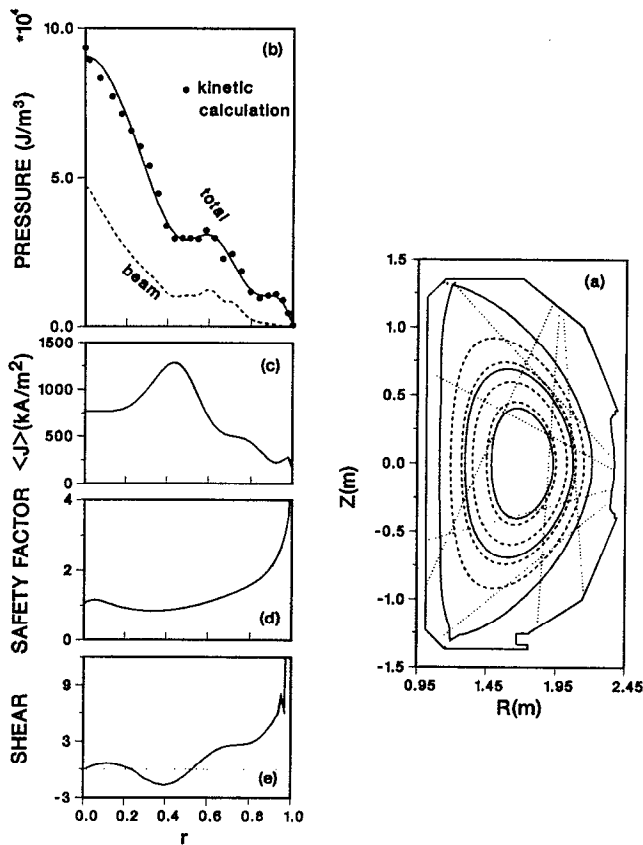
FIG. 15. Symmetrized equilibrium calculation for 69608, allowing for flat regions in the T_i profile as described in the text. (a) Flux surface contours. The inner solid contours are the $q=1$ surfaces and the dotted lines are the soft x-ray chords on which the peak $m/n=1/1$ activity is observed. (b) The pressure versus normalized radius. The solid line it the best fit in the reconstruction, the solid circles are the calculated pressure based on the profile data, and the dashed line is the calculated fast ion component. (c) The flux surface averaged toroidal current density, (d) the safety factor, and (e) the shear.

netic axis location. The pressure profile is constrained to match the new kinetic calculation. Here ff' is constrained to reproduce l_i. In addition, q_0 and edge current density are constrained to locate the inner and outer $q=1$ surfaces. The best solution is shown in Fig. 15 and compared to the equilibrium reconstruction of Fig. 11 in Table III.

We believe the reconstruction shown in Fig. 11 to be the more accurate representation of global parameters, as it represents a true χ^2 minimization, without the errors introduced by the symmetrization. However, as discussed in the next section, from the viewpoint of stability analysis the inclusion of the flat region in the pressure profile is an essential feature of this plasma, and this is the best match we have been able to achieve to all the features of the experiment.

IV. STABILITY ANALYSIS

A. Ballooning stability

The stability against the high toroidal mode number ideal ballooning mode is evaluated using the MBC[30] and the

TABLE III. Comparison of the best-fit and symmetrized equilibria for DIII-D discharge 69608 at $t=1417$ msec.

	Fit	Symmetrized
Major radius, R_0 (m)	1.67	1.66
Magnetic axis, R_m (m)	1.76	1.75
Minor radius, a (m)	0.56	0.55
Elongation, κ	2.34	2.39
Axial elongation, $\kappa(0)$	2	2
Triangularity, δ	0.84	0.85
Plasma volume, m^{-3}	21.0	20.2
Toroidal beta, β_T (%)	11.2	10.3
Poloidal beta, β_P	0.96	0.94
Internal inductance, l_i	0.91	0.91
$p_0/\bar{p}$	3.8	3.7
ψ at inner $q=1$	0.13	0.15
ψ at outer $q=1$	0.53	0.54

CAMINO[31] codes. The effects of fast ions have been included in the equilibrium reconstruction, but finite Larmor radius effects are not included in the stability analysis. The ballooning analysis shows four distinct zones in the plasma with spatial location, as indicated by different line segments in the normalized midplane pressure profile shown in Fig. 16.

A number of symmetrized MHD equilibria were calculated, which provided a good match to the data of the experimental discharge averaged in time ± 5 msec about the time of maximum beta value was calculated. These equilibria varied somewhat in how well they matched the experimental results, however, the essential features of the ballooning stability are insensitive to these variations. Only the spatial extent of the zones described here changed in these analyses.

We use the behavior of the specific equilibrium shown in Fig. 15 to discuss the general characteristics of these equilibria. The safety factor, $q(\tilde{\psi})$, and pressure gradient, $p'(\tilde{\psi})$, are shown in Fig. 17. In the outer portion of the
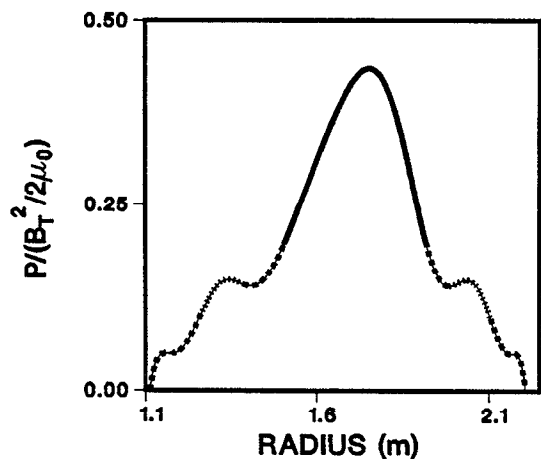

FIG. 16. The midplane pressure profile. Pressure is normalized to the toroidal field at the magnetic axis [$B_T(R_m=1.75$ m$)=0.724$ T]. The differing line segments correspond to the four stability zones described in the text and shown in Fig. 18.

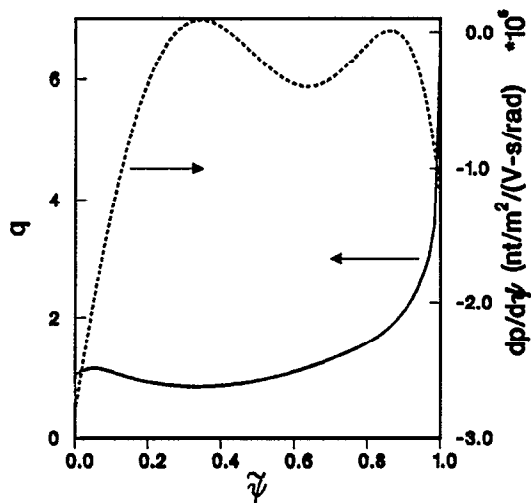FIG. 17. Here q vs $\tilde{\psi}$ and p' vs $\tilde{\psi}$ from the equilibrium shown in Fig. 15.

FIG. 18. (a), (b), (c), (d) The $s\text{-}\alpha$ for representative surfaces in zones 1–4, with s and α defined as follows: $\rho = \sqrt{V(\psi)/(2\pi^2 R_m)}$, $s=2\partial(\ln q)/\partial(\ln V)$, $\alpha=\mu_0\rho p'(\psi)\,V'(\psi)/(2\pi^2)$. The regions of ballooning and Mercier instability are shown. The experimental data point is given by the solid circle. The Mercier unstable zone is cross-hatched and the ballooning unstable zone is dotted. (a) $\tilde{\psi}$=0.71, (b) $\tilde{\psi}$=0.41, (c) $\tilde{\psi}$=0.21, and (d) $\tilde{\psi}$=0.07.

plasma, $\tilde{\psi}>0.35$, q increases with the poloidal flux. This is the positive shear region, which is the typical behavior of the q profile for an ordinary tokamak. In the inner region, $\tilde{\psi}<0.35$, the q profile decreases from the center toward the outside. This is the negative shear region, which is the typical q profile for a stellarator or an elongated tokamak. Note that in this particular example, there is a second small ($\tilde{\psi}<0.05$) positive shear region. Other cases with slightly greater q_0 did not show this feature, and we do not consider it to be consequential. The $q=1$ surfaces are located at $\tilde{\psi}=0.15$ and $\tilde{\psi}=0.50$. The region close to the transition between the positive and negative shear zones has a small but non-negligible shear.

The general behavior of the pressure gradient profile is shown in Fig. 17. It is seen that the pressure gradient is very large (and negative) in the central region of the plasma. It increases (its magnitude decreases) to around zero throughout the region enclosed by the $q=1$ surfaces, reflecting, primarily, the change in the temperature gradient. It then increases up to a moderate value and decreases again to a small value at the location of the $q=2$ surface. This flattening is largely a reflection of the density profile. Finally, its magnitude increases to a large value at the plasma edge.

The general behavior of the ballooning stability diagram may be classified into the following four types. In the outer positive shear region ($\tilde{\psi}>0.35$), two different types of diagrams are possible. When there is a local magnetic well (favorable average field line curvature), the plasma pressure gradient can be increased in a flux conserving manner while avoiding Mercier instability; but increasing the local pressure gradient can result in ballooning instability. The plasma in the outer region is in the first ballooning stable regime. This is typified by the $s\text{-}\alpha$ diagram of flux surface at $\tilde{\psi}=0.71$ shown in Fig. 18(a). It is seen that the experimental point is close to the stability boundary. With a further increase of the pressure gradient on this surface (moving to the right), the flux surface will become ballooning unstable. When there is no magnetic well (unfa-
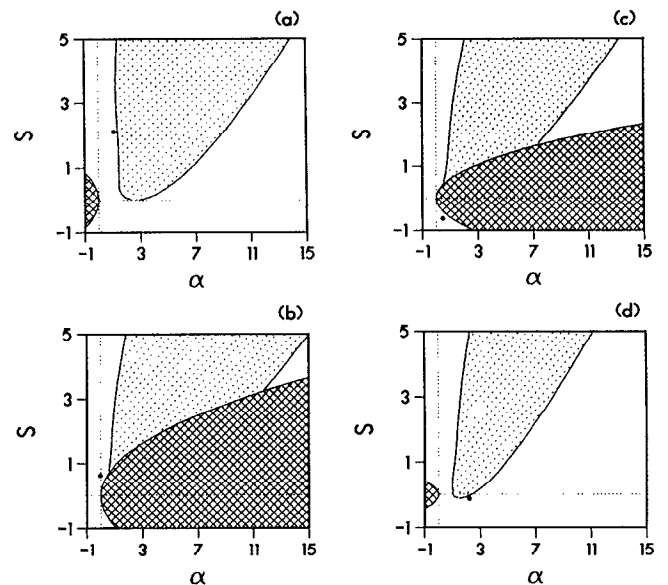
vorable average field line curvature), which is the case for surfaces with q less than a critical value,[32] $q_c\approx 1$ ($0.15<\tilde{\psi}<0.50$), a Mercier instability region appears in the $\alpha>0$ side of the stability diagram. This is typified by the behavior of the stability diagram of surface at $\tilde{\psi}=0.41$ shown in Fig. 18(b). The Mercier unstable zone is inside the parabola. We see that the experimental point marked by a solid circle is outside of this region, also due to the low pressure gradient and its (relatively high) shear.

Moving further into the plasma ($0.05<\tilde{\psi}<0.35$), the shear is negative. Again, depending on the sign of the local magnetic well, there are two different possible types of stability diagrams. For the region with smaller q, the Mercier stability boundary appears on the $\alpha>0$ side of the stability diagram. This is typified by the behavior of the surface at $\tilde{\psi}=0.21$. As can be seen from the diagram [Fig. 18(c)] the plasma surface data point would be moved into the Mercier unstable zone if the shear of the surface decreases or its pressure gradient increases. These plasma surfaces are stable through their shear. Further inward toward the magnetic axis ($\tilde{\psi}<0.15$), the q value increases further, there is a local magnetic well, and the Mercier unstable region changes from the $\alpha>0$ side to the $\alpha<0$ side of the stability diagram. The plasma surface then enters into the second stable region at the center. This is typified by the surface located at $\tilde{\psi}=0.07$ shown in Fig. 18(d). Note that the reversed magnetic shear is the key factor that produces the second stable core. In the second stable zone the pressure gradient is more than twice the first stability limit.

We thus see that this discharge achieves ballooning stability with a high beta by developing a first regime edge and a second regime core. These two regions are connected
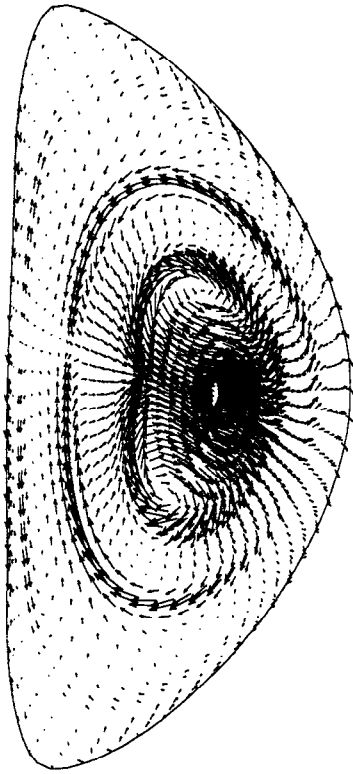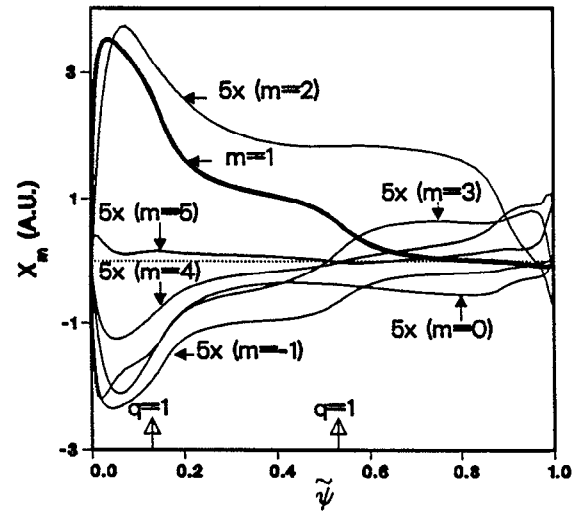
FIG. 20. Poloidal Fourier decomposition of the perpendicular component, $X = \xi \cdot \nabla \Psi / |\nabla \Psi|$, of the displacement shown in Fig. 19. In the interest of clarity, poloidal harmonics $m > 5$, whose amplitude is less than 5% of the $m = 1$ amplitude, are not shown. These higher harmonics are finite only near the plasma edge. The $m = 1$ component is shown as a thick line. The other components are scaled in amplitude by a factor of 5 for clarity.

FIG. 19. Linearized displacement vectors, ξ, projected onto the poloidal plane, for the $n = 1$ kink mode computed by the GATO code for shot 69608. The arrows indicate the direction and relative magnitude of the unstable displacement at every fourth grid point used in the calculation.

by a low pressure gradient region so as to remain stable to the Mercier stability criterion. Since the plasma surfaces have not yet achieved marginal pressure gradients with respect to the ballooning modes everywhere in the first stable zones, it is conceivable that the edge and central pressure gradients may be further increased, leading to a further increase in the achievable beta value.

B. Kink stability

Ideal kink stability analysis using GATO[10] predicts that the equilibrium is linearly unstable to what is essentially an $n = 1$ ideal internal mode (Fig. 19). Fourier analysis of the normal displacement is shown in Fig. 20. The unstable mode is most accurately described as a toroidal kink[33] superimposed on a quasi-interchange mode.[34] The quasi-interchange component is due to the hollow q profile and, in Fig. 20, this is reflected in the overall parabolic dependence of the $m = 1$ harmonic with the flux coordinate. The toroidal kink component is a result of the fact that the minimum in the q profile is significantly less than unity, which is well known to destabilize a true internal kink at sufficiently high β, and the fact that the stabilizing wall is not on the plasma surface but is at the real DIII-D wall location. The latter allows the characteristic toroidal kinklike coupling of $m > 2$ external kinklike Fourier harmonics with the $m = 1$, $m = 2$ internal kink structure; the

growth rate with the real DIII-D wall is a factor 4 higher than that of the pure internal mode (the wall placed on the plasma surface).

The amplitudes of the $m = 4$, $m = 5$ components are the dominant harmonics at the edge. The relative amplitudes of these external kinklike components compared to the internal structure is known to sensitively depend on the details of the current density at the edge. These details are not well known in the experiment. In the equilibrium calculation, the edge current density (along with q_0) are free parameters adjusted to match the total plasma current and the l_i value while matching the location of the $q = 1$ surfaces. The maximum edge displacement is only about 15% of the peak internal displacement. The flux surface displacements shown in Fig. 21 indicate that the boundary hardly moves relative to the center; in fact, there is relatively little displacement of the flux surfaces outside the second $q = 1$ surface. The instability would, therefore, not be expected to disrupt the plasma on a linear ideal MHD time scale.

Normally, a true internal kink or toroidal kink is thought to result in a periodic internal reorganization of the plasma inside $q = 1$ in a sawtoothlike fashion. However, the unstable mode predicted by the linear stability code has an unusual structure and, with the presence of two $q = 1$ surfaces, the usual nonlinear sawtooth mechanisms are not necessarily applicable. It is, therefore, conceivable that this particular mode could nonlinearly saturate at a finite amplitude, consistent with the saturated $n = 1$ internal mode that was observed in the experiment. Note that this mode structure is also consistent with the observed SXR data in the qualitative sense that there should be considerable MHD activity at both $q = 1$ surfaces—the kinetic energy
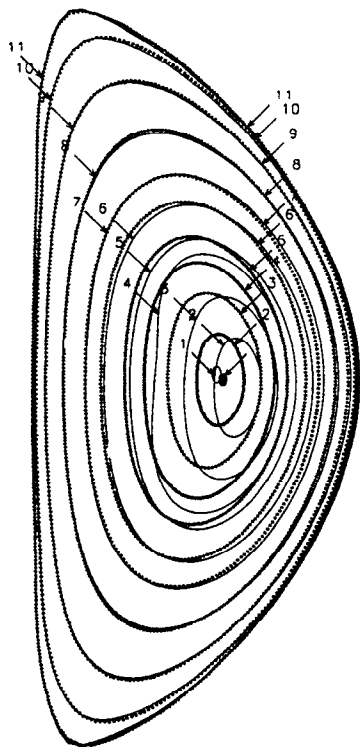
FIG. 21. Displacement of the equilibrium flux surfaces under the perturbation shown in Fig. 19. The scale of the displacement is an arbitrary constant. The initial equilibrium contours are shown as the numerically labeled dotted curves and the corresponding perturbed flux surfaces are the solid curves. The two $q=1$ surfaces correspond closely to those contours labeled as 4 and 7 and the $q=2$ surface corresponds to the contour labeled 9. Note the relatively small displacement of the plasma outside the outer $q=1$ surface.
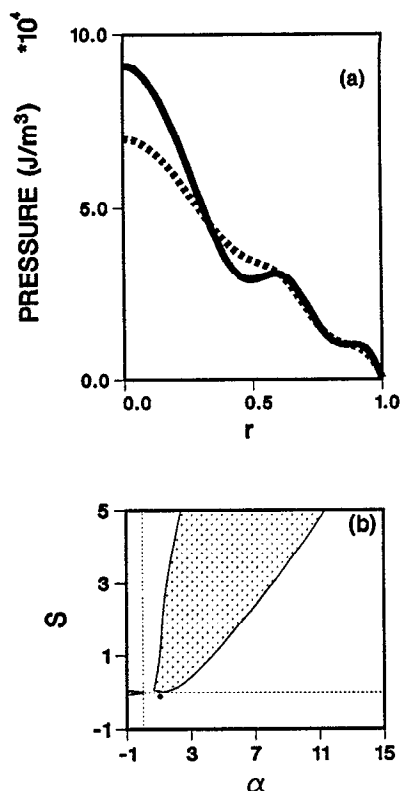
FIG. 22. Error analysis for ballooning stability. (a) Pressure profile. The solid curve is the pressure profile used in the original analysis. The dashed curve is an extreme of the experimental uncertainties that minimizes p' inside the inner $q=1$ surface; and (b) the S-α diagram for $\tilde{\psi}=0.07$ with this pressure profile.

contours are strongly localized at these surfaces (see Fig. 19, for example). This would not be true, for example, if the predicted mode were a true internal (or toroidal) kink or a true quasi-interchange mode.

C. Axisymmetric stability

The results show that the plasma is stable to the $n=0$ axisymmetric mode with a conducting wall located at the vacuum vessel surrounding the plasma. If the radius of the vessel is increased by 11%, the plasma then becomes unstable, indicating that an additional increase in the elongation κ of several percent in these discharges to further optimize $\mathcal{S}$ is possible.

D. Error analysis of ballooning stability

To complete this section we wish to address the accuracy of the conclusion that the core of the plasma is second stable. Possibly, even though not observed, there are anomalous losses of central fast ion pressure, and the profile is broader than our analysis indicates. One possibility is to simply estimate the uncertainties in S and α for the data point shown in Fig. 17(d), and for nearby flux surfaces. The problem with this approach is that the errors are not constrained to be consistent with an equilibrium, and furthermore, this would ignore the consequent change in the

stability boundary in S-α space. Instead, to estimate the uncertainty, we will need to generate a new equilibrium and examine its stability.

In generating this equilibrium we will attempt to reduce p' in the central region to a minimum conceivable value. The SXR emissivity profile (Fig. 12) has calibration uncertainties of 3%. By systematically adjusting the data points one can conclude that the magnetic axis could be 0.30–0.05 m inside of that from our best analysis. One might further speculate that the emissivity is not a totally reliable measure of the magnetic axis location and take the center of the inner $q=1$ surface to be the magnetic axis, and thus set $p_0/\langle p\rangle = 3$. We have computed such an equilibrium, with a peak beta of 33%. The $q=1$ surface are still constrained at their previous location (Table III). In doing this we obtain an equilibrium with $p_0/\langle p\rangle = 3$ and a magnetic axis located at $R=1.72$ m, shifted inward by 0.04 m from our previously calculated axis location. The pressure profile is shown in Fig. 22(a).

The stability analysis for this equilibrium still shows that the interior region is second stable. When compared to the data point in Fig. 17(d), at $\tilde{\psi}=0.07$, the stability boundary has moved slightly upward while the data point has moved down and to the left, as shown in Fig. 22(b). Here p' is 1.7 times the first stable limit for this equilibrium. Moving the locations of the $q=1$ surfaces would
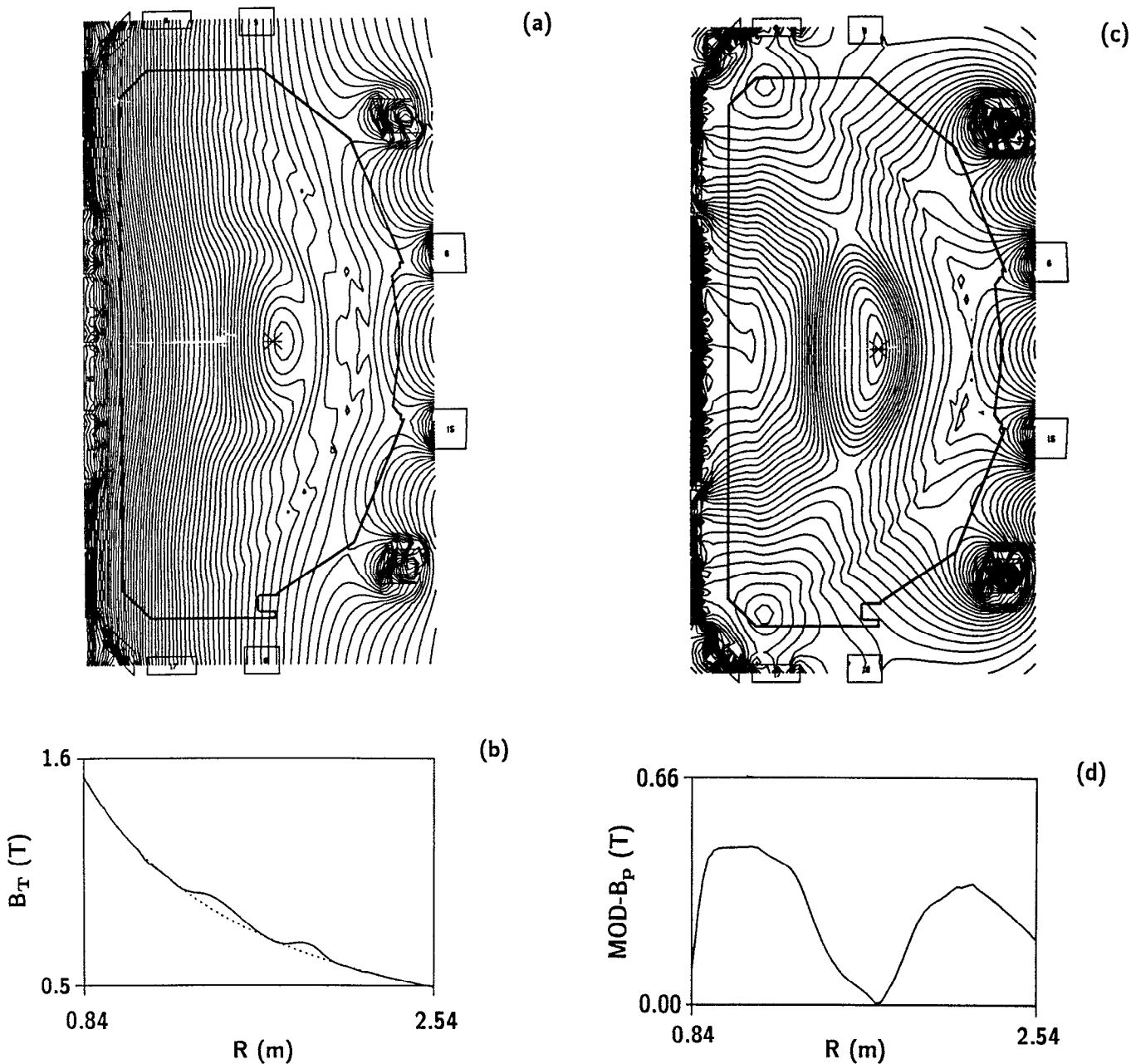
FIG. 23. Field strength for 69608 at 1417 msec using the equilibrium shown in Fig. 15: (a) mod-B contours, (b) the midplane toroidal field with the vacuum field shown as a dotted line, (c) mod-B_p contours, and (d) the midplane slice of mod-B_p. The contours are equally spaced in field strength. The asterisk denotes the magnetic axis.

simply change the volume of the second stable region, as discussed in Sec. IV A.

V. THE ISODYNAMICAL EQUILIBRIUM LIMIT

Having produced this plasma with its second-stable core, it is logical to pursue the issue of increasing the central pressure. From the viewpoint of ballooning stability, the central pressure can be increased without limit provided the q profile remains similar, and p' still vanishes somewhere within the region where $q < 1$.

As mentioned previously, central mod-B surfaces are closed, and the plasma is close to isodynamical (omnige-

nous) near the magnetic axis. Isodynamical equilibria, that is equilibria where B is constant on a flux surface, were first discussed by Palumbo.[35] In Fig. 23(a) we show contours of mod-B, which close in the plasma interior. The asterisk denotes the magnetic axis. Note from the midplane toroidal field [Fig. 23(b)] that, although $\beta_p \approx 1$, there is considerable variation in the flux function $f(\psi)$. Also, note in the mod-B_p contours [Fig. 23(c)] that there is no indication of the formation of a separatrix inside of the magnetic axis, although the poloidal field is clearly [Fig. 23(d)] becoming weak there.

If we were to attempt to take further advantage of the

second stability of the core, say by increasing the central heating, an increase in central beta would increase $p_0/\langle p \rangle$, and thus Δ_m [Eq. (2)], bringing the mod-B surfaces into closer alignment with the flux surfaces. However, a system with a curved magnetic axis cannot be isodynamical at the magnetic axis unless either the magnetic field vanishes ($q_0 = 0$) or the flux surfaces do not close.[36] We believe this plasma is close to this isodynamical equilibrium limit. The proof of this limit in Ref. 36 is accomplished by an expansion of the MHD equations about the magnetic axis; as such, it provides no information nor criterion for how close a plasma may come to this limit nor what to expect as a relaxation phenomenon.

We find that, if we try to modify the experimental equilibrium by raising central pressure as little as 8%, the equilibrium solution fails to converge. We had concluded in Ref. 2 that an increase of beta to 13% would make the core omnigenous. Our present standards for satisfactory convergence are considerably more stringent than they were at that time. For the reasons discussed in the next paragraph we no longer believe that the conclusion was correct.

Rather than deal with the complexity of this particular solution, we have pursued this issue with more idealized profiles while maintaining the plasma current, toroidal field, and similar shape. We choose the form $p_0'(1 - \tilde{\psi})^4$ for p' and specify ff' as a third-order polynomial in $\tilde{\psi}$. Here ff' is constrained by four conditions; $q_0 = 1.1$, total plasma current, the current density vanish at the separatrix, and the ratio of the constant to the linear term is specified, so as to obtain a hollow current profile and an l_i value that is similar to the experiment. This is done in a fixed-boundary calculation. We then increase p_0 (and β_p) until the solution fails to converge. Flux and mod-B contours for the highest beta (10.2%) solution that converged are shown in Fig. 24. Note that the offset of central flux and mod-B surfaces is similar to that found in the experiment (Fig. 23). This procedure was repeated using $p_0'(1 - \tilde{\psi})^5$ and a similar result was found. Convergence was achieved up to $\beta_T = 8.3\%$ and the central relationship of closed mod-B surfaces to the magnetic axis was the same, as shown here. We also note that there is no difficulty obtaining good solutions at extremely high beta values, provided that the pressure profile is broad and the central mod-B contours are not aligned with the flux surfaces. Similarly, the difficulties in generating equilibria disappear if we choose to constrain $q_0 \approx 0$. Finally, the results are not changed significantly if we change the computational mesh size.

We cannot claim on the basis of lack of convergence of a solution in an equilibrium code that we have actually reached this limit, but it is clear that the experiment is quite close to it and in a practical sense may well have reached this limit. This result also serves to further explain the difficulty we experienced in generating an accurate equilibrium reconstruction of the experimental results.

Motivated by the indications of a pressure-related equilibrium limit, which were seen in the equilibrium reconstruction calculations, we have searched for evidence of such a limit in the behavior of the discharge. Since this is a local axial limit to the equilibrium, we expected a relaxation of the central portion of the discharge accompanied by a $m/n = 1/0$ radial oscillation, rather than a disruption or other catastrophic event. We do not find any compelling evidence for this type of relaxation. This limit will be the subject of further theoretical and experimental work. Interestingly, for both this plasma and those just prior to and after it, we do see an $m = 1$ radial oscillation at the time of peak beta, but we do not see any unique signature for shot 69608. There remains a possibility that the small sawtooth-like events in 69608 discussed in Sec. III are a manifestation of this limit.

VI. DISCUSSION

Although the experiment contained a number of interesting new results, in terms of global parameters the results confirmed our expectation, as discussed in Sec. II, that is the results are consistent with Troyon scaling.[3] We have produced a beta value of 11% in a highly elongated, H-mode plasma. The intent of the experiment was to operate at the intersection of the axisymmetric and external kink boundaries with maximum $\mathscr{S}$, thus achieving a maximum beta value. The shot disrupted due to an external kink, although it was close to the axisymmetric limit. The achieved value $\mathscr{S} = 8.0$ was close to the expected value of 8.25. While we have not proven that the increase in beta over the 9.3% achieved in the full-radius DND configuration ($\mathscr{S} = 7.2$) was explicitly due to the shape change, the results do support this viewpoint. In experiments, when comparable beam power was injected the plasma either disrupted or there was no further increase in beta over that achieved with 16 MW of beam power. The value of normalized beta, $\beta_N = 3.7$, achieved here is slightly higher than that achieved at $q \lesssim 3$ in either the single-null divertor or the DND configurations. However, the l_i value is 0.91, somewhat higher than the expected value of 0.81. This is consistent with the observation[11] that in DIII-D, $\beta_N \approx 4l_i$. In this experiment we avoided the usual dramatic decrease in beta at the occurrence of the first ELM. We also note that, although much effort has been expended on beta studies in the single-null configuration ($\mathscr{S} = 5.4$), the maximum beta achieved has been 7.4%. Taken together, these results support the hypothesis that the shape factor, which is bounded by axisymmetric stability and the low-q limit taken together determine the maximum achievable beta.

There is an implication in these results that the second stable core might be a requirement for achieving the 11% beta, in that 69609 only reached 9.2% beta. We do not believe that one should draw this conclusion. In doing high beta experiments, it is by definition the case that many plasmas reach less than the maximum beta. A great deal more operating time would be required before such a conclusion could be drawn.

The most interesting result is that of a high central pressure. The central pressure in this discharge is 3.8 times the volume average. Here
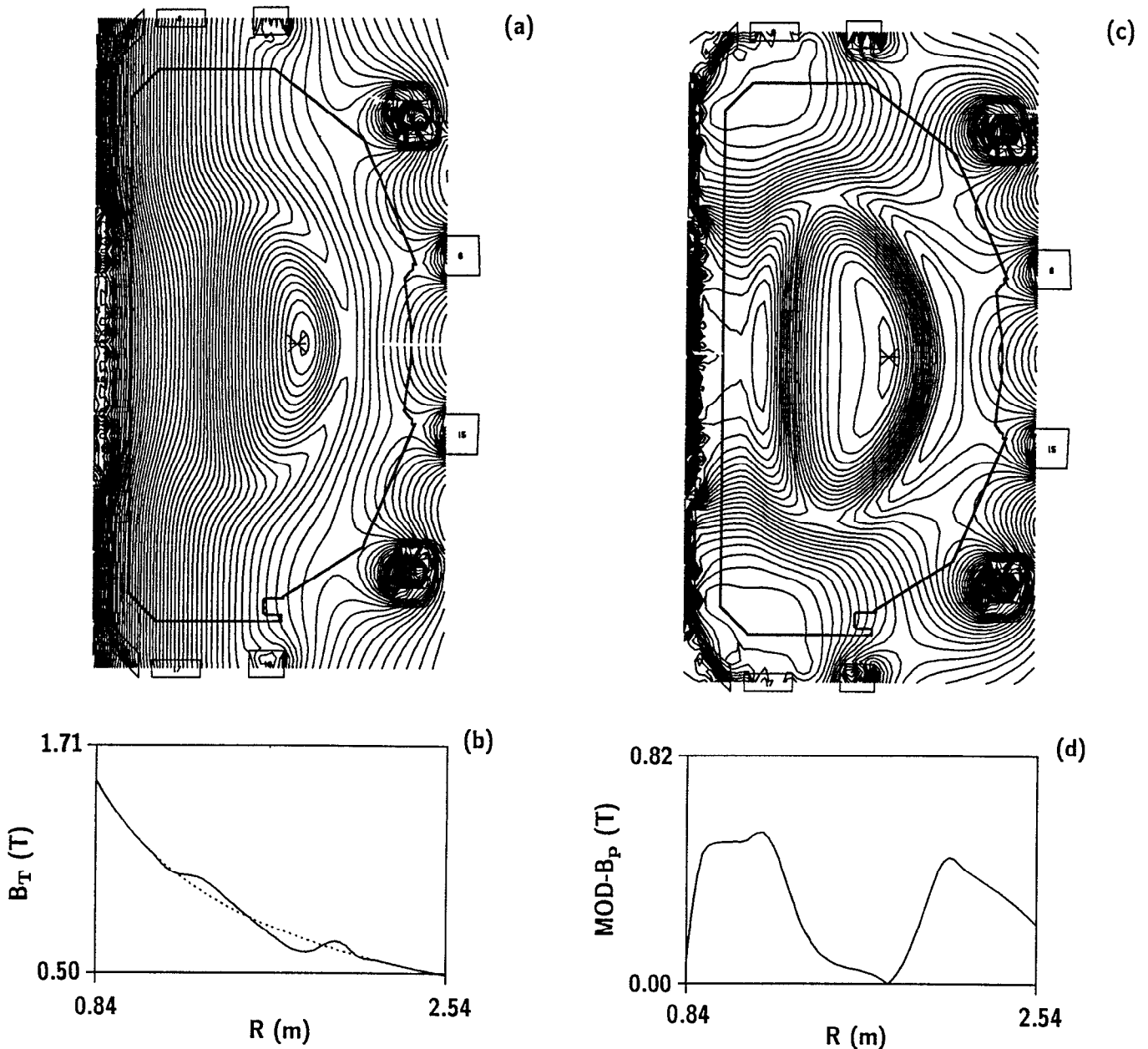
FIG. 24. Field strength for a pressure profile $p_0(1-\psi)^4$ at the maximum pressure for which the equilibrium calculation converges as discussed in the text: (a) mod-B contours, (b) the midplane toroidal field with the vacuum field shown as a dotted line, (c) mod-B_p contours, and (d) the midplane slice of mod-B_p. The contours are equally spaced in field strength. The asterisk denotes the magnetic axis.

$$\beta^* \left(\equiv \frac{2\mu_0}{B_T^2} \sqrt{\frac{\int p^2 \, dV}{\int dV}} \right),$$

a more realistic measure of fusion reactivity than β_T, is 15%. Second stability is a necessity in reaching this state, as the first stable boundary (Fig. 2) results in $p_0/\langle p \rangle \approx 2$. The peaked pressure profile is normally more characteristic of higher edge q plasmas, such as the hot ion H-mode discharges,[37] and has not been previously observed at these low values of the safety factor. In fact, this plasma had an even more peaked pressure profile than did the hot ion H-mode discharges, which reaches $p_0/\langle p \rangle \sim 3.2$. There is

evidence that the plasma reached the isodynamical equilibrium limit. This conclusion is tentative and more theoretical and experimental work is required.

It is not clear why the central region remains at $q_0 > 1$. Assuming the toroidal electric field from the transformer is radially uniform across the plasma, and a reasonable resistivity profile the maintenance of such an equilibrium requires some mechanism to produce the necessary modification of the toroidal electric field. This mechanism might be that the time derivative of the magnetic field be nonzero (MHD activity) or a bootstrap current. From the soft x

rays it is clear that the amplitude of the perturbation in the two $m=1$ islands is anticorrelated. Perhaps the interaction of these two islands provides reconnection, destroying poloidal flux before it reaches the magnetic axis, thus eliminating the need for central reconnection. Theoretically such behavior is possible.[38]

We have not drawn a conclusion as to exactly why p' vanishes within the $q < 1$ region. While this feature is necessary for preserving Mercier stability, it does not follow that the flattening is due to an interchange. Double tearing is also a candidate, as is simply the existence of the $m/n = 1/1$ structures. It is interesting that we designed an equilibrium where we could not find a solution with a monotonic q profile and, as we approach these conditions experimentally, the discharge 69608 exhibited this behavior. Of course, the following discharge, 69609, did not show such behavior, but it was not at as high a beta.

It is clear from the comparison of shots 69608 and 69609 that the avoidance of reconnection in the central region is important, in that it allows the central pressure to increase. The existence of the internal kink is not surprising, since both β_p and κ are destabilizing to this mode.[39,40] The increase in pressure profile peakedness is consistent with the observation on ISX-B[41] that the electron temperature profile was more peaked, with a higher $T_e(0)$ in the presence of the continuous internal kink than in a sawtoothing discharge.[42] To our knowledge this is the first observation of a second stable core plasma in a tokamak. The results appear qualitatively similar to the second stability reported[43] in the ATF stellarator.[44]

At the time of completing this manuscript we have been afforded an opportunity to operate similar discharges. We are pleased to report that we have reproduced the plasma of 69608. While a full analysis is several months away, we did reach at least as high a beta value and we did observe a double saturated internal mode. Perhaps most importantly, in support of the analysis presented here, we found the density profile to be hollow with very high gradients at the edge and a flat central region comparable to that shown in Fig. 10.

We shall attempt with a rather simple, and somewhat incomplete, approach to offer a qualitative interpretation of what we believe to be the essential physics of this plasma. In reality the plasma described here is very complex; in a rigorous sense it is not axisymmetric. Furthermore, we believe that the double $m/n = 1/1$ island structure is an important aspect of the experiment. Thus an accurate description would have multiple magnetic axes.

The discharge begins as a conventional tokamak plasma. We then begin a second current ramp while starting neutral beam heating at the 5 MW level and increasing the elongation. The discharge begins this interval in a sawtoothing mode, which indicates $q_0 < 1$. Both the increase in β_p (heating) and the increase in κ serve to destabilize the internal kink, and a saturated mode appears. The double island structure undergoes reconnection and acts as a barrier, preventing the added current of the second ramp from penetrating to the interior. At the same time the increasing internal elongation raises q_0 above unity. Arriving at this

situation may depend quite sensitively on the timing of the shaping and NBI relative to the last sawtooth crash. However arrived at, this condition provides a q profile that permits a second stable core. Then the high-powered neutral beam injection (19 MW) overcomes transport losses and the central pressure rises rapidly. This continues until the core plasma reaches the isodynamical equilibrium limit at the magnetic axis. Approximately 4 of the 19 MW of injected beam power is deposited within the inner $q=1$ surface. Bootstrap current associated with the high-pressure gradient of the second stable region may help to maintain the hollow current density and q profile.

In summary, we have found a regime in operating space that allows operation near the intersection of the $n=0$ and $n=1$ ideal stability limits in DIII-D. Within this operating constraint in these strongly shaped plasmas we have found a regime of high central beta with a second stable plasma core. This regime permits high central pressure while maintaining stability against the devastating global kink modes. There is evidence that the plasma reached the isodynamical equilibrium limit. Assuming this to be the case, the plasma performance is then limited by equilibrium, $n=0$, and $n=1$ ideal stability. Although the global confinement was poor ($\tau_E \approx 40$ msec) the plasma parameters are not limited by transport.

We believe that, with the appropriate current profile control, we can maintain the negative central shear over a wider range of elongation and at higher values of the safety factor. We look forward to pursuing this line of research in the near future.

[1] J. L. Luxon and G. L. Davis, Fusion Technol. 8, 441 (1985).
[2] E. A. Lazarus, M. S. Chu, J. R. Ferron, F. J. Helton, J. T. Hogan, A. G. Kellman, L. L. Lao, J. B. Lister, T. H. Osborne, R. Snider, E. J. Strait, T. S. Taylor, and A. D. Turnbull, Phys. Fluids B 3, 2220 (1991).
[3] F. Troyon, R. Gruber, H. Saurenmann, S. Semenzato, and S. Succi, Plasma Phys. Controlled Fusion 26, 209 (1984).
[4] A. Sykes, M. F. Turner, and S. Patel, Proceedings of the 11th European Conference on Controlled Fusion and Plasma Physics 1983, Aachen (European Physical Society, Petit-Lancy, Switzerland, 1983), Vol. 2, p. 363.
[5] J. R. Ferron, M. S. Chu, F. J. Helton, W. Howl, A. G. Kellman, L. L. Lao, E. A. Lazarus, J. K. Lee, T. H. Osborne, E. J. Strait, T. S. Taylor, and A. D. Turnbull, Phys. Fluids B 2, 1280 (1990).

[6]E. A. Lazarus, J. B. Lister, and G. H. Neilson, Nucl. Fusion 30, 111 (1990).

[7]J. B. Lister, E. A. Lazarus, A. G. Kellman, J.-M. Moret, J. R. Ferron, F. J. Helton, L. L. Lao, J. A. Leuer, E. J. Strait, T. S. Taylor, and A. D. Turnbull, Nucl. Fusion 30, 2349 (1990).

[8]E. A. Lazarus, A. D. Turnbull, A. G. Kellman, J. R. Ferron, F. J. Helton, L. L. Lao, J. A. Leuer, E. J. Strait, and T. S. Taylor, *Proceedings of the 11th European Conference on Controlled Fusion and Plasma Physics 1990*, Amsterdam (European Physical Society, Petit-Lancy, Switzerland, 1990), Vol. 1, p. 427.

[9]J. M. Greene and M. S. Chance, Nucl. Fusion 21, 453 (1981); K. Yamazaki, H. Naitou, T. Amano, Y. Hamada, K. Matsuoka, Y. Midzuno, Y. Nakayama, and T. Sato, *Plasma Physics and Controlled Nuclear Fusion Research*, Kyoto, 1986 (International Atomic Energy Agency, Vienna, 1987), Vol. II, p. 27.

[10]L. C. Bernard, F. J. Helton, and R. W. Moore, Comput. Phys. Commun. 24, 377 (1981).

[11]T. S. Taylor, E. A. Lazarus, M. S. Chu, J. R. Ferron, F. J. Helton, W. Howl, G. L. Jackson, T. H. Jensen, Y. Kamada, A. G. Kellman, L. L. Lao, R. J. LaHaye, J. A. Leuer, J. B. Lister, T. H. Osborne, R. Snider, R. D. Stambaugh, E. J. Strait, and A. D. Turnbull, in *Plasma Physics and Controlled Nuclear Fusion Research*, Washington, 1990 (International Atomic Energy Agency, Vienna, 1990), Vol. 1, p. 177.

[12]F. B. Marcus, J. M. Adams, A. Cheeaham, S. Conroy, W. G. F. Core, O. N. Jarvis, M. J. Loughlin, M. Olsson, G. Sadler, P. Smeulders, P. van Belle, and N. Watkins, *Proceedings of the 11th European Conference on Controlled Fusion and Plasma Physics 1990*, Amsterdam (European Physical Society, Petit-Lancy, Switzerland, 1990), Vol. 1, p. 331.

[13]K. McGuire, R. Goldston, M. Bell, M. Bitter, K. Bol, K. Brau, D. Buchenaur, T. Crowley, S. Davis, F. Dylla, H. Eubank, H. Fishman, R. Fonck, B. Grek, R. Grimm, R. Hawryluk, H. Hsuan, R. Hulse, R. Izzo, R. Kaita, S. Kaye, H. Kugel, D. Johnson, J. Manickam, D. Manos, D. Mansfield, E. Mazzucatto, R. McCann, D. McCune, D. Monticello, R. Motley, D. Mueller, K. Oasa, M. Okabayashi, K. Owens, W. Park, M. Reusch, N. Sauthoff, G. Schmidt, S. Sesnic, J. Strachan, C. Surko, R. Slusher, H. Takahashi, F. Tenney, P. Thomas, H. Towner, J. Valley, and R. White, Phys. Rev. Lett. 50, 891 (1983).

[14]B. B. Kadomtsev, Sov. J. Plasma Phys. 1, 389 (1975).

[15]W. Pfeiffer, Nucl. Fusion 25, 673 (1985).

[16]D. J. Campbell, J. G. Cordey, A. W. Edwards, R. D. Gill, E. Lazzaro, G. Maygar, A. L. McCarthy, J. O'Rourke, F. Pegararo, F. Porcelli, P. Smeulders, D. F. H. Start, P. Stubberfield, J. A. Wesson, E. Westerhof, and D. Zasche, *Plasma Physics and Controlled Nuclear Fusion Research*, Vienna, 1988 (International Atomic Energy Agency, Vienna, 1989), Vol. II, p. 377.

[17]L. L. Lao, J. R. Ferron, R. J. Groebner, W. Howl, H. St. John, E. J. Strait, and T. S. Taylor, Nucl. Fusion 30, 1035 (1990).

[18]G. L. Jackson, J. Winter, S. Lippmann, T. W. Petrie, J. C. DeBoo, J. R. Ferron, D. N. Hill, D. P. Schissel, and T. S. Taylor, J. Nucl. Mater. 165, 139 (1990).

[19]D. Wroblewski, K. H. Burrell, L. L. Lao, P. Politzer, and W. P. West, Rev. Sci. Instrum. 61, 3552 (1990).

[20]D. Wroblewski and L. L. Lao, Phys. Fluids B 3, 2877 (1990).

[21]W. W. Pfeiffer, Nucl. Fusion 25, 655 (1985), and references contained within.

[22]R. N. Morris, R. H. Fowler, J. A. Rome, and T. J. Schlagel, Fusion Technol. 12, 281 (1987), and references contained therein.

[23]W. W. Heidbrink, J. Kim, and R. J. Groebner, Nucl. Fusion 28, 1897 (1988).

[24]W. W. Heidbrink, Phys. Fluids B 2, 4 (1990).

[25]P. C. Efthimion, M. Bitter, E. D. Fredrickson, R. J. Goldston, G. W. Hammett, K. W. Hill, H. Hsuan, R. A. Hulse, R. Kaita, D. K. Mansfield, D. C. McCune, K. M. McGuire, S. S. Medley, D. Mueller, A. T. Ramsey, S. D. Scott, B. C. Stratton, K.-L. Wong, the TFTR Group, H. Biglari, P. H. Diamond, Y. Takase, and V. A. Vershkov, *Plasma Physics and Controlled Nuclear Fusion Research*, Vienna, 1988 (International Atomic Energy Agency, Vienna, 1989).

[26]W. W. Heidbrink, C. W. Barnes, G. W. Hammett, Y. Kusama, S. D. Scott, M. C. Zarnstorff, L. C. Johnson, D. McCune, S. S. Medley, H. K. Park, A. L. Roquemore, J. D. Strachan, and G. Taylor, Phys. Fluids B 3, 3167 (1991).

[27]S. D. Scott, C. W. Barnes, L. R. Grisham, G. Hammett, D. W. Johnson, Y. Kusama, M. C. Zarnstorff, S. J. Zweben, M. G. Bell, M. Bitter, R. Boivin, R. Budny, C. E. Bush, A. Cavallo, C. Z. Cheng, V. Decaux, P. C. Efthimion, R. J. Fonck, E. Fredrickson, R. J. Goldston, B. Grek, R. J. Hawryluk, K. W. Hill, H. Hsuan, A. Janos, D. Jassby, F. C. Jobes, L. C. Johnson, R. Kaita, S. Kaye, P. H. LaMarche, B. LeBlanc, D. K. Mansfield, D. C. McCune, K. M. McGuire, S. S. Medley, D. Mueller, J. Murphy, D. K. Owens, H. Park, P. Perkins, S. Pitcher, A. T. Ramsey, A. L. Roquemore, J. Schivell, G. L. Schmidt, B. C. Stratton, W. Stodiek, E. Synakowski, W. Tang, G. Taylor, H. H. Towner, S. von Goeler, R. Waltz, R. Wieland, M. Williams, and K. M. Young, *Plasma Physics and Controlled Nuclear Fusion Research*, Washington, 1990 (International Atomic Energy Agency, Vienna, 1990), Vol. 1, p. 235.

[28]L. L. Lao, H. St. John, and R. D. Stambaugh, Nucl. Fusion 25, 1421 (1985).

[29]L. A. Artsimovitch, Nucl. Fusion 12, 215 (1972). Equation (3.10) contains a typographical error and should read $\lambda(r)=[8\pi/H_\varphi^2(r)][\bar{p}(r)-p(r)]+l_i(r)/2$.

[30]R. W. Moore, R. R. Dominguez, and M. S. Chu, Nucl. Fusion 25, 1575 (1985).

[31]M. S. Chance, *Proceedings of Theory of Fusion Plasma*, Varenna, 1987 (Societa Italiana di Fisca, Bologna, Italy, 1988), Vol. 18, p. 87.

[32]F. J. Helton, J. M. Greene, T. Ohkawa, P. A. Politzer, and A. D. Turnbull, Nucl. Fusion 31, 487 (1991).

[33]A. D. Turnbull and F. Troyon, Nucl. Fusion 29, 1887 (1989).

[34]J. A. Wesson, Plasma Phys. Controlled Fusion 28, 243 (1986).

[35]D. Palumbo, Nuovo Cimento 53B, 507 (1967).

[36]M. P. Bernardin, R. W. Moses, and J. A. Tataronis, Phys. Fluids 29, 2605 (1986).

[37]K. H. Burrell, R. J. Groebner, T. S. Kurki-Suonio, T. N. Carlstrom, R. R. Dominguez, P. Gohil, R. A. Jong, H. Matsumoto, J. M. Lohr, T. W. Petrie, G. D. Porter, G. T. Sager, H. E. St. John, D. P. Schissel, and S. M. Wolfe, *Plasma Physics and Controlled Nuclear Fusion Research*, Washington, 1990 (International Atomic Energy Agency, Vienna, 1990), Vol. 1, p. 123.

[38]B. A. Carreras, H. R. Hicks, and B. V. Waddell, Nucl. Fusion 19, 583 (1979).

[39]J. L. Dunlap, B. A. Carreras, V. K. Paré, J. A. Holmes, S. C. Bates, J. D. Bell, H. R. Hicks, V. E. Lynch, and A. P. Navarro, Phys. Rev. Lett. 48, 539 (1982).

[40]J. Manickam, Nucl. Fusion 24, 595 (1984).

[41]M. J. Saltmarsh, J. Vac. Sci. Technol. 17, 260 (1980).

[42]E. A. Lazarus, J. D. Bell, C. E. Bush, A. Carnevali, B. A. Carreras, W. H. Casson, J. L. Dunlap, P. H. Edmonds, A. C. England, W. L. Gardner, G. A. Hallock, J. T. Hogan, H. C. Howe, D. P. Hutchinson, R. R. Kindsfather, R. C. Isler, P. K. Mioduszewski, M. Murakami, G. H. Nielson, V. K. Pare, D. J. Sigmar, C. E. Thomas, R. M. Wieland, J. B. Wilgen, W. R. Wing, A. J. Wootton, and K. E. Yokoyama, Nucl. Fusion 25, 135 (1985).

[43]J. H. Harris, M. Murakami, B. A. Carreras, J. D. Bell, G. L. Bell, T. S. Bigelow, L. A. Charlton, N. Dominguez, J. L. Dunlap, J. C. Glowienka, L. D. Horton, H. C. Howe, R. C. Isler, H. Kaneko, R. R. Kindsfather, J. N. Leboeuf, V. E. Lynch, M. M. Menon, R. N. Morris, G. H. Nielson, V. K. Paré, D. A. Rasmussen, J. B. Wilgen, and W. R. Wing, Phys. Rev. Lett. 63, 1249 (1989).

[44]J. F. Lyon, B. A. Carreras, K. K. Chipley, M. J. Cole, J. H. Harris, T. C. Jeringan, R. L. Johnson, V. E. Lynch, B. E. Nelson, J. A. Rome, J. Sheffield, and P. B. Thompson, Fusion Technol. 10, 179 (1986).